A novel mesh regularization approach based on finite element distortion potentials: Application to material expansion processes with extreme volume change

Abhiroop Satheesh [*], Christoph P. Schmidt, Wolfgang A. Wall, Christoph Meier

Institute for Computational Mechanics, Technical University of Munich, Garching, 85748, Germany

ARTICLE INFO

ABSTRACT

The accuracy of finite element solutions is closely tied to the mesh quality. In particular, geometrically nonlinear problems involving large and strongly localized deformations often result in prohibitively large element distortions. In this work, we propose a novel mesh regularization approach allowing to restore a non-distorted high-quality mesh in an adaptive manner without the need for expensive re-meshing procedures. The core idea of this approach lies in the definition of a finite element distortion potential considering contributions from different distortion modes such as skewness and aspect ratio of the elements. The regularized mesh is found by minimization of this potential. Moreover, based on the concept of spatial localization functions, the method allows to specify tailored requirements on mesh resolution and quality for regions with strongly localized mechanical deformation and mesh distortion. In addition, while existing mesh regularization schemes often keep the boundary nodes of the discretization fixed, we propose a mesh-sliding algorithm based on variationally consistent mortar methods allowing for an unrestricted tangential motion of nodes along the problem boundary. Especially for problems involving significant surface deformation (e.g., frictional contact), this approach allows for an improved mesh relaxation as compared to schemes with fixed boundary nodes. To transfer data such as tensor-valued history variables of the material model from the old (distorted) to the new (regularized) mesh, a structure-preserving invariant interpolation scheme for second-order tensors is employed, which has been proposed in our previous work and is designed to preserve important properties of tensor-valued data such as objectivity and positive definiteness. As a practically relevant application scenario, we consider the thermo-mechanical expansion of materials such as foams involving extreme volume changes by up to two orders of magnitude along with large and strongly localized strains as well as thermo-mechanical contact interaction. For this scenario, it is demonstrated that the proposed regularization approach preserves a high mesh quality at small computational costs. In contrast, simulations without mesh adaption are shown to lead to significant mesh distortion, deteriorating result quality, and, eventually, to non-convergence of the numerical solution scheme.

---

* Corresponding author.
  E-mail addresses: abhiroop.satheesh@tum.de (A. Satheesh), christoph.schmidt@tum.de (C.P. Schmidt), wolfgang.a.wall@tum.de (W.A. Wall),
christoph.anton.meier@tum.de (C. Meier).

1. Introduction

The accuracy of finite element solutions is closely tied to the quality of the underlying finite element mesh. Excessive element distortions can result in unreliable solutions or even lead to divergence. Therefore, it is important to keep mesh distortions small to achieve accurate and reliable results. To address this issue, dynamic mesh treatment techniques have been developed and studied. In general, replacing the old mesh by a newly generated mesh (i.e., remeshing) is typically a computationally inefficient approach, especially in 3D, as it results in high computational costs and challenges regarding parallel communication. In addition, the inherent challenges of producing high-quality meshes for complex geometries are re-occurring in every remeshing step, which also means that it requires additional means for maintaining mesh quality. In contrast, mesh adaptation, i.e. moving element nodes while keeping the number of nodes and their connectivity fixed in the sense of r-refinement, allows for updating the mesh without consuming excessive computational resources. For many applications, this seems to be a more efficient approach. Mesh adaptation typically consists of two major steps viz. finding the new nodal positions (new mesh) and transferring data from the old to the new mesh. In this work, we term the first step as *mesh refitting* and the second step as *data transfer*, while the overall procedure including both steps is termed *mesh adaptation*.

Mesh refitting techniques have been studied in the past, e.g., in the context of fluid–structure interaction based on arbitrary Lagrangian–Eulerian (ALE) discretizations. These methods can be classified as interpolation and physical analogy-based methods. A detailed review of mesh refitting methods can be found in [1]. In interpolation-based schemes, an interpolation function is used to obtain the new mesh and in general they do not require nodal connectivity information, which enables their application to polyhedral elements or unstructured grids. The most common methods in this category are transfinite interpolation [2], the algebraic damping method [3], and radial basis function interpolation [4]. Transfinite interpolation has the disadvantage of (potentially) producing inverted elements, while the algebraic damping method may yield non-smooth aspect ratio distributions in the domain. Additionally, the use of radial basis function methods can be computationally expensive. In contrast, physical analogy-based methods use the element connectivity information and find the new nodal positions by solving a system of equations formulated according to a physical process. The first approach in this class is the linear spring analogy scheme proposed by Batina [5]. In this method, a fictitious spring is added to the discretization with a stiffness inversely proportional to the element edge length. This method frequently results in inverted elements and is less suited for large deformation problems. To prevent element inversion, modified spring analogies such as torsional spring [6], semi-torsional spring [7], ball-vertex [8], and ortho-semi-torsional spring approaches were proposed. However, these methods are either limited to triangular elements (respectively, tetrahedral elements in 3D) or have been shown to exhibit poor performance for large deformation problems. Moreover, these methods can also result in inverted elements or boundary nodes that are not relaxed. Another set of methods in this group is given by Laplacian methods [9,10], in which a Laplace equation is solved in the interior of the domain. These schemes allow for a certain degree of regularization for distorted meshes and they ensure that the interior nodes remain confined by the domain boundaries. However, Laplacian methods often result in a limited mesh movement, i.e., a limited mesh regularization, and may also lead to inverted elements (see [10]). Finally, in an elastostatic approach [11,12], the discretized domain is considered as an elastic body and the new nodal locations are obtained through the solution of an elasticity problem. Here, the new nodal positions are dependent on the values of Young's modulus and Poisson's ratio underlying the pseudo-elastic problem. Yet, a linear elastostatic equation can lead to inverted elements and non-linear constitutive equations can lead to poor element quality for large deformation problems. Improved elastostatic approaches can be found in [13–15]. Still, these methods typically suffer from insufficient element quality control and are not well-suited for large deformation problems with localized mesh distortion.

In summary, there is still a need for mesh refitting techniques that can produce a high quality mesh for problems involving very large and strongly localized deformation. Existing methods tend to give either inverted elements or elements with low quality in such scenarios. Moreover, controlling the element size and quality at specific regions of the domain is not easily feasible with existing approaches. In addition, the mesh movement for boundary nodes is either limited or for some approaches even impossible, leading to distorted elements at the boundary.

Once the new mesh is obtained, the primary and history variables must be mapped from the old to the new mesh. The accuracy of the data mapping between the meshes is critical for all adaptive FEM procedures. The most common data types that arise as history variables are scalars and tensors. On the one hand, the mapping of scalar variables is well investigated, and methods such as moving least squares can be adopted [16–21]. On the other hand, the mapping of tensor-valued data was not well-studied before [22]. To bridge this gap, structure preserving tensor interpolation schemes have been proposed and evaluated in our previous work [22]. These interpolation schemes fulfill essential properties of the underlying continuum mechanics problem such as objectivity, positive definiteness, and monotonicity of invariants of the interpolated tensors along with higher-order spatial convergence.

To overcome the aforementioned limitations of existing approaches, we propose a novel mesh adaptation scheme. The underlying mesh refitting approach is based on the definition of an element distortion potential considering contributions from different distortion modes such as skewness and aspect ratio of the elements. The regularized mesh is obtained by minimizing this potential. Moreover, based on the concept of spatial localization functions, the method allows to specify tailored requirements on mesh resolution and quality for regions with strongly localized mechanical deformation and mesh distortion. To address also problems involving significant surface deformation, we propose the usage of a mortar mesh-sliding scheme to allow for a tangential motion of boundary nodes without changing the boundary topology. It is demonstrated that this approach enables a significantly improved mesh relaxation as compared to schemes with fixed boundary nodes. To transfer tensor-valued history data from the old to the new mesh, we utilize the structure-preserving interpolation methods proposed in our previous work [22]. The effectiveness of the proposed scheme is validated by means of several selected numerical examples. In particular, as a practically relevant application
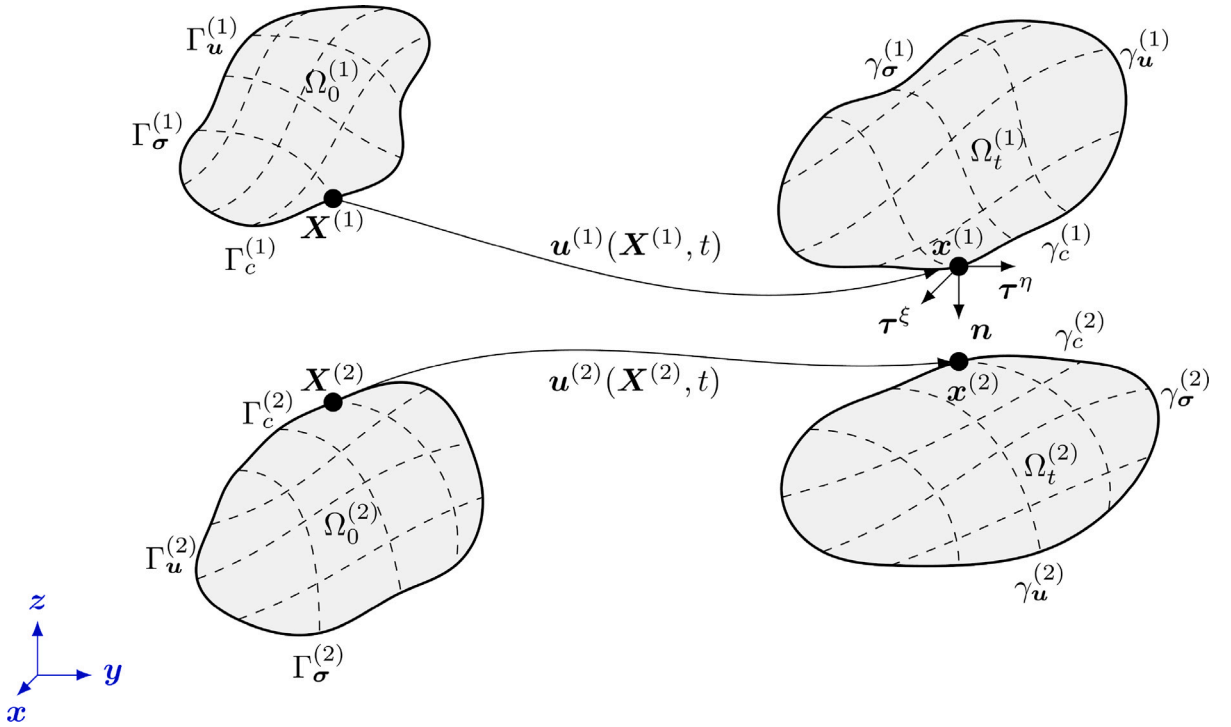
Fig. 1. Notation and kinematics to depict the interaction between two deformable bodies.

scenario, we consider the thermo-mechanical expansion of materials such as foams involving extreme volume changes by up to two orders of magnitude along with large and strongly localized strains as well as thermo-mechanical contact interaction. For this scenario it is demonstrated that the proposed regularization approach preserves a high mesh quality at small computational costs. In the investigated numerical examples, the computation time for mesh adaptation was typically in the order of only a few percent of the total simulation time. In contrast, simulations without mesh adaption are shown to lead to significant mesh distortion and, eventually, to non-convergence of the numerical solution scheme.

The remainder of this work is organized as follows: While the main novelty of the work, the overall mesh adaptation approach, can be applied to all kinds of problems, we demonstrate it using thermomechanical problems driven by the demands from specific applications. To ease presentation, we first introduce this problem class and related methods in Section 2 before presenting the mesh adaptation in Section 3. In particular, the finite-strain inelastic material model is introduced in Section 2.2, followed by the considered mortar methods for thermo-mechanical contact in Section 2.3, and finally discretization in space and time in Section 2.4. Next, the mesh adaptation method is detailed in Section 3, in which the mesh refitting problem is formulated in Section 3.1, and the data transfer methods are described in Section 3.2. Finally, selected numerical examples are presented in Section 4 and the main novelties and findings of this work are summarized in Section 5.

2. Thermo-mechanical problem

In this work, we propose a novel mesh adaption method, which is able to regularize strongly distorted meshes without the need for a complete remeshing. While the proposed method is very general, in this work as a demonstration example it is applied to a finite deformation thermo-mechanical problem involving thermally activated materials undergoing very large (inelastic) volume expansion as well as thermo-mechanical contact interaction, which typically results in prohibitively large mesh distortions if no mesh adaption is applied. We start with a description of the underlying thermo-mechanical problem. Next, the thermo-mechanical constitutive model for the inelastic expansion is presented, followed by the thermo-mechanical contact formulation.

2.1. Thermo-mechanical initial boundary value problem

Consider the deformation of bodies $i = \{1, 2\}$ with reference configuration $\boldsymbol{X}^{(i)} \in \Omega_0^{(i)}$ and current configuration $\boldsymbol{x}^{(i)} \in \Omega_t^{(i)}$ at time t described by the mapping $\varphi_t^{(i)} : \boldsymbol{X}^{(i)} \mapsto \boldsymbol{x}^{(i)}$ as illustrated in Fig. 1. The displacement $\boldsymbol{u}^{(i)}$ at material point $\boldsymbol{X}^{(i)}$ is given by $\boldsymbol{u}^{(i)}(\boldsymbol{X}^{(i)}, t) = \boldsymbol{x}^{(i)}(\boldsymbol{X}^{(i)}, t) - \boldsymbol{X}^{(i)}$ and the temperature is denoted by $T^{(i)}(\boldsymbol{X}^{(i)}, t)$. The thermo-mechanical initial boundary value problem (IBVP) summarizing the set of equations required to determine the displacement and temperature field, i.e. the primary variables

$\boldsymbol{u}^{(i)}$ and $T^{(i)}$ in the time interval $t \in [0, t^E]$, reads:

$$
\begin{aligned}
\nabla_{\boldsymbol{X}} \cdot (\boldsymbol{F}^{(i)} \boldsymbol{S}^{(i)}) + \hat{\boldsymbol{b}}_0^{(i)} &= \rho_0^{(i)} \ddot{\boldsymbol{u}}^{(i)} && \text{in } \Omega_0^{(i)} \times [0, t^E], \\
-\nabla_{\boldsymbol{X}} \cdot \boldsymbol{Q}^{(i)} + \hat{R}_0^{(i)} &= c_v^{(i)} \dot{T}^{(i)} && \text{in } \Omega_0^{(i)} \times [0, t^E], \\
(\boldsymbol{F}^{(i)} \boldsymbol{S}^{(i)}) \boldsymbol{N}^{(i)} &= \hat{\boldsymbol{t}}_0^{(i)} && \text{on } \Gamma_\sigma^{(i)} \times [0, t^E], \\
\boldsymbol{Q}^{(i)} \cdot \boldsymbol{N}^{(i)} &= \hat{Q}_0^{(i)} && \text{on } \Gamma_q^{(i)} \times [0, t^E], \\
\boldsymbol{u}^{(i)} &= \hat{\boldsymbol{u}}^{(i)} && \text{on } \Gamma_u^{(i)} \times [0, t^E], \\
T^{(i)} &= \hat{T}^{(i)} && \text{on } \Gamma_T^{(i)} \times [0, t^E], \\
\boldsymbol{\sigma}^{(i)} \boldsymbol{n}^{(i)} &= \boldsymbol{t}_c^{(i)} && \text{on } \gamma_c^{(i)} \times [0, t^E], \\
\boldsymbol{q}^{(i)} \cdot \boldsymbol{n}^{(i)} &= q_c^{(i)} && \text{on } \gamma_c^{(i)} \times [0, t^E], \\
\boldsymbol{u}^{(i)} &= \boldsymbol{u}_0^{(i)} && \text{in } \Omega_0^{(i)} \text{ for } t = 0, \\
\dot{\boldsymbol{u}}^{(i)} &= \dot{\boldsymbol{u}}_0^{(i)} && \text{in } \Omega_0^{(i)} \text{ for } t = 0, \\
T^{(i)} &= T_0^{(i)} && \text{in } \Omega_0^{(i)} \text{ for } t = 0,
\end{aligned}
\tag{1}
$$

where $\dot{(\cdot)}$ is the total time derivative, $\nabla_{\boldsymbol{X}}$ the gradient with respect to the material position vector $\boldsymbol{X}$, $\hat{\boldsymbol{b}}_0^{(i)}$ the body forces per unit reference volume, $\rho_0^{(i)}$ the mass density per unit reference volume, $\hat{R}_0^{(i)}$ the heat source per unit reference volume, and $c_v^{(i)}$ the specific heat capacity. $\boldsymbol{N}$ and $\boldsymbol{n}$ represent outward unit-normal vectors onto the surfaces of the considered bodies in material and spatial description, respectively. Furthermore, $\boldsymbol{F}$, $\boldsymbol{S}$, $\boldsymbol{\sigma}$, $\boldsymbol{Q}$, and $\boldsymbol{q}$ are the deformation gradient, second Piola–Kirchhoff stress tensor, Cauchy stress tensor, material heat flux, and spatial heat flux, respectively, and are detailed in the following sections. The first two equations in (1) are the momentum balance and the heat conduction equation, respectively. The Neumann boundary conditions for the mechanical problem on $\Gamma_\sigma^{(i)}$ and for the thermal problem on $\Gamma_q^{(i)}$ involve the prescribed fluxes $\hat{\boldsymbol{t}}_0^{(i)}$ and $\hat{Q}_0^{(i)}$. The Dirichlet boundary conditions for the mechanical problem on $\Gamma_u^{(i)}$ and for the thermal problem on $\Gamma_T^{(i)}$ are represented by the prescribed values $\hat{\boldsymbol{u}}^{(i)}$ and $\hat{T}^{(i)}$, respectively. The next two equations correspond to the Cauchy traction $\boldsymbol{t}_c^{(i)}$ and Cauchy heat flux $q_c^{(i)}$ at the contact surfaces $\gamma_c^{(i)}$. Finally, $\boldsymbol{u}_0^{(i)}$, $\dot{\boldsymbol{u}}_0^{(i)}$, and $T_0^{(i)}$ depict the initial conditions of the displacement, velocity, and temperature, respectively.

For the subsequent finite element formulation, first the weak form of the coupled thermo-mechanical IBVP is formulated. The weak form is obtained by multiplying the linear momentum and heat conduction equations in (1) with test functions $\delta \boldsymbol{u}^{(i)}$ and $\delta T^{(i)}$, respectively, then integrating over the domains, and applying Green's theorem. Eventually, the weak forms of the mechanical and thermal problem without contact contribution read

$$
\underbrace{\int_{\Omega^{(i)}} \rho_0^{(i)} \, \delta \boldsymbol{u}^{(i)} \cdot \ddot{\boldsymbol{u}}^{(i)} \, \mathrm{d}\Omega}_{\delta \mathcal{W}_u^{\text{iner}}} + \underbrace{\int_{\Omega^{(i)}} \nabla_{\boldsymbol{X}} \delta \boldsymbol{u}^{(i)} : (\boldsymbol{F}^{(i)} \boldsymbol{S}^{(i)}) \, \mathrm{d}\Omega}_{\delta \mathcal{W}_u^{\text{int}}} - \underbrace{\left(\int_{\Omega^{(i)}} \delta \boldsymbol{u}^{(i)} \cdot \hat{\boldsymbol{b}}_0^{(i)} \, \mathrm{d}\Omega + \int_{\Gamma_\sigma^{(i)}} \delta \boldsymbol{u}^{(i)} \cdot \hat{\boldsymbol{t}}_0^{(i)} \, \mathrm{d}\Gamma \right)}_{\delta \mathcal{W}_u^{\text{ext}}} = 0
\tag{2}
$$

and $\underbrace{\int_{\Omega^{(i)}} \delta T^{(i)} c_v^{(i)} \dot{T}^{(i)} \, \mathrm{d}\Omega}_{\delta \mathcal{W}_T^{\text{iner}}} + \underbrace{\int_{\Omega^{(i)}} \nabla_{\boldsymbol{X}} \delta T^{(i)} \cdot \boldsymbol{Q}^{(i)} \, \mathrm{d}\Omega}_{\delta \mathcal{W}_T^{\text{int}}} - \underbrace{\left(\int_{\Omega^{(i)}} \delta T^{(i)} \hat{R}_0^{(i)} \, \mathrm{d}\Omega + \int_{\Gamma_q^{(i)}} \delta T^{(i)} \hat{Q}_0^{(i)} \, \mathrm{d}\Gamma \right)}_{\delta \mathcal{W}_T^{\text{ext}}} = 0,$

$$\tag{3}$$

respectively, wherein $\delta \mathcal{W}_u^{\text{iner}}$, $\delta \mathcal{W}_u^{\text{int}}$, and $\delta \mathcal{W}_u^{\text{ext}}$ are the mechanical inertia, internal, and external virtual work contributions, respectively, and the corresponding virtual work contributions of the thermal problem are denoted by $\delta \mathcal{W}_T^{\text{iner}}$, $\delta \mathcal{W}_T^{\text{int}}$, and $\delta \mathcal{W}_T^{\text{ext}}$.

2.2. Kinematics and constitutive model for large deformation thermo-mechanical problem

The mesh adaptation method proposed in Section 3 is motivated by one of our current research questions involving material behavior with extreme volume expansion. Since the proposed mesh adaption scheme is independent of the specific form of the material law, and also for reasons of confidentiality by our industrial partner, the constitutive law governing the inelastic volume expansion, i.e., the function $f(T, \boldsymbol{S}, \alpha)$ in Eq. (6), will be stated in a generic form below.

Following the framework of nonlinear continuum mechanics, the local deformation at a material point $\boldsymbol{X}$ is described by the deformation gradient $\boldsymbol{F} = \frac{\partial \boldsymbol{x}}{\partial \boldsymbol{X}}$. To account for inelastic deformations, we adopt the multiplicative split of the deformation gradient into an elastic part $\boldsymbol{F}_e$ and an inelastic part $\boldsymbol{F}_{in}$ as proposed by Lee [23] in the context of plasticity:

$$
\boldsymbol{F} = \boldsymbol{F}_e \boldsymbol{F}_{in}.
\tag{4}
$$

We allow for an anisotropic inelastic volume expansion with respect to the principal stretch directions $\boldsymbol{N}_C^i$, which are given by the eigenvectors of the right Cauchy–Green stretch tensor $\boldsymbol{C} = \boldsymbol{F}^{\mathrm{T}} \boldsymbol{F}$, according to

$$
\boldsymbol{F}_{in} = \sum_{i=1}^{3} \lambda_{in}^i \boldsymbol{N}_C^i \otimes \boldsymbol{N}_C^i,
\tag{5}
$$

where λ_{in}^i is the magnitude of the inelastic expansion in the direction $\boldsymbol{N}_C^i$, governed by an evolution equation

$$
\dot{\lambda}_{in}^i = f(T, \boldsymbol{S}, \alpha),
\tag{6}
$$

accounting for dependencies of the inelastic volume expansion on the current temperature, stress state and on the scalar-valued internal variable α governing the material history. Exemplarily, the scalar α can be a material degradation factor which reduces from 1 to 0 during the expansion process. In the numerical examples studied in this work, we prescribe α as an explicit function of time. Finally, a similar definition of inelastic deformation material models can be found in the context of biomechanics: e.g., a stress-dependent growth model was presented by Rodriguez et al. in [24], and Lubarda and Hoger showcased isotropic and anisotropic stress-modulated growth in [25].

In analogy to the (total) right Cauchy–Green stretch tensor C, the *elastic* right Cauchy–Green stretch tensor is defined as $C_e = F_e^{\mathrm{T}} F_e$. Based on C_e, we define a hyperelastic strain–energy function $\Psi_e(C_e)$ under the assumption that the elastic response does not explicitly depend on the temperature. Based on this assumption and the multiplicative split (4), the second Piola–Kirchhoff stress tensor S can be computed as (see [26] for more details)

$$S = 2 F_{in}^{-1} \frac{\partial \Psi_e}{\partial C_e} F_{in}^{-\mathrm{T}}. \tag{7}$$

Furthermore, the spatial Cauchy stress tensor σ follows as $\sigma = (\det F)^{-1} F S F^{\mathrm{T}}$. In the examples presented in this paper, the hyperelastic strain–energy function is based on a Neo-Hookean model as presented in [26].

Finally, the thermal constitutive equation relating heat flux and temperature gradient via the isotropic heat conductivity k_0 is formulated on the basis of Fourier's law. The latter can be stated using either the (material) second Piola–Kirchhoff heat flux Q or the spatial heat flux $q = (\det F)^{-1} F Q$ according to

$$Q = -k_0 C^{-1} \nabla_X T \quad \text{or} \quad q = -\frac{k_0}{\det F} \nabla_x T, \tag{8}$$

where we distinguish between the material gradient $\nabla_X = \frac{\partial}{\partial X}$ and the spatial gradient $\nabla_x = \frac{\partial}{\partial x}$.

2.3. Thermo-mechanical contact

In this section, we discuss the thermo-mechanical contact formulation used in this work. The underlying contact constraints along with the basics of mortar methods for constraint enforcement and regularization are briefly summarized below. For a detailed description of these mortar methods in the context of thermomechanical contact interaction, the interested reader is referred to exemplary literature [27,28]. While the general formulation accounts for frictional contact interaction, for simplicity, only the frictionless case will be recapitulated in the following.

2.3.1. Mechanical contact problem: Kinematics and contact forces

In the following, we distinguish the contacting surfaces as master and slave side denoted by the sets $\mathcal{M}$ and $\mathcal{S}$, respectively. Here, a superscript (1) refers to the slave side and $\gamma_c^{(1)}$ represents the contact surface on the slave side. The relative motion between these interfaces at any time instant t is quantified by the smooth mapping (see Fig. 1)

$$\chi_t(\boldsymbol{x}^{(1)}) : \gamma_c^{(1)} \to \gamma_c^{(2)}, \boldsymbol{x}^{(1)} \mapsto \boldsymbol{x}^{(2)}. \tag{9}$$

This mapping projects any point $\boldsymbol{x}^{(1)}$ from the slave surface $\gamma_c^{(1)}$ onto the master surface $\gamma_c^{(2)}$ along the outward normal $\boldsymbol{n}(\boldsymbol{x}^{(1)})$ or in short $\boldsymbol{n}$ (see Fig. 1). The unit vectors spanning the tangential plane at the contact point are denoted as $\boldsymbol{\tau}^\eta$ and $\boldsymbol{\tau}^\xi$. The mapping is assumed to exist in the zone of closed contact and its close vicinity. For (potentially) interacting points on the slave surface $\gamma_c^{(1)}$, the normal gap is defined as

$$g_n(\boldsymbol{x}^{(1)}) = -\boldsymbol{n} \cdot [\boldsymbol{x}^{(1)} - \boldsymbol{x}^{(2)}]. \tag{10}$$

Moreover, the traction vectors acting on the contact surfaces are denoted as $\boldsymbol{t}_c^{(i)}$. Based on a balance of linear momentum, the traction vectors on the slave and master side of the contact surface are related according to $\boldsymbol{t}_c^{(1)} = -\boldsymbol{t}_c^{(2)} =: \boldsymbol{t}_c$. Furthermore, the contact traction can be decomposed into a normal component $p_n^{(i)}$ and a tangential component $\boldsymbol{t}_\tau^{(i)}$:

$$p_n^{(i)} = \boldsymbol{n} \cdot \boldsymbol{t}_c^{(i)}, \tag{11}$$

$$\boldsymbol{t}_\tau^{(i)} = (\boldsymbol{I} - \boldsymbol{n} \otimes \boldsymbol{n}) \boldsymbol{t}_c^{(i)}. \tag{12}$$

2.3.2. Mechanical contact problem: Constraints and virtual work

The (frictionless) mechanical contact constraints are given by the Hertz–Signorini–Moreau conditions:

$$g_n \geq 0, \quad p_n \leq 0, \quad p_n g_n = 0 \quad \text{on } \gamma_c^{(1)}. \tag{13}$$

As basis for a variational statement of the contact problem, the slave side traction vector $\boldsymbol{t}_c$ is introduced as an additional primary field, which is identified as Lagrange multiplier $\boldsymbol{\lambda}_c = -\boldsymbol{t}_c$ associated with the contact constraint. If the normal component of the Lagrange multiplier is denoted as $\lambda_{c,n} = \boldsymbol{n} \cdot \boldsymbol{\lambda}_c$, the contact virtual work can be shown to yield:

$$\delta \mathcal{W}_u^c = -\int_{\gamma_c^{(1)}} [\![\delta \boldsymbol{u}]\!] \cdot \boldsymbol{\lambda}_c \, \mathrm{d}\gamma = \int_{\gamma_c^{(1)}} \delta g_n \lambda_{c,n} \, \mathrm{d}\gamma, \tag{14}$$

where $[\![\cdot]\!] = (\cdot)^{(1)} - [(\cdot)^{(2)} \circ \chi_t]$ is the jump operator (cf. (9)) and δg_n the variation of the normal gap in (10).

2.3.3. Thermal contact problem

Next, the thermal effects at the contacting surfaces have to be addressed. The heat balance at the interface reads

$$q_c^{(1)} + q_c^{(2)} = 0, \tag{15}$$

with $q_c^{(1)}$ and $q_c^{(2)}$ being the slave and master side heat fluxes across the contact interface defined according to (cf. (8))

$$q_c^{(i)} = \boldsymbol{q}^{(i)} \cdot \boldsymbol{n}^{(i)}. \tag{16}$$

Within this work, an interface heat flux model with a linear dependence on the contact pressure is used according to

$$q_c^{(1)} = \beta_c |p_n| [\![T]\!], \quad q_c^{(2)} = -\beta_c |p_n| [\![T]\!], \tag{17}$$

where $\beta_c \geq 0$ is the contact heat conductivity. Finally, the virtual work of the interface heat conduction problem reads:

$$\delta \mathcal{W}_T^c = - \int_{\gamma_c^{(1)}} q_c^{(1)} [\![\delta T]\!] \mathrm{d}\gamma, \tag{18}$$

Therein, all contact integrals are transformed into pure slave side integrals using (9). As studied in [27–29], it is not necessary to introduce thermal Lagrange multipliers $\lambda_T = -q_c^{(1)}$ to enforce the thermal interface constraints. Instead, a direct substitution of the heat flux model (17) into (18) allows to express the interface heat fluxes as function of the temperature, which is the primary variable of the thermal problem.

Remark 2.3.1. The drawback of this direct heat flux substitution method is that the problem becomes ill-conditioned for very large values of β_c, i.e., in the limit $\beta_c \rightarrow \infty$. In this case, alternative approaches such as the Lagrange multiplier method [30] or Nitsche's method [31] are well suited.

2.4. Discretization in space and time

The displacement and temperature field are approximated in space through trial functions defined on basis of discrete nodal values $\mathbf{d}_j$ and $\mathbf{T}_j$ and ansatz functions N_j, whereas the Lagrange multiplier field is approximated in space through trial functions defined on basis of discrete nodal values $\boldsymbol{\Lambda}_{c,j}$ and ansatz functions ϕ_j, viz

$$\boldsymbol{u}^h = \sum_{j=1}^{n} N_j \mathbf{d}_j, \quad T^h = \sum_{j=1}^{n} N_j \mathbf{T}_j, \quad \lambda_c^h = \sum_{j \in S} \phi_j \boldsymbol{\Lambda}_{c,j}. \tag{19}$$

In (19) the global vectors $\mathbf{d}$ and $\mathbf{T}$ contain all displacement and temperature degrees of freedom, respectively and the vector $\boldsymbol{\Lambda}_c$ all nodal Lagrange multipliers. The corresponding test functions can be written as

$$\delta \boldsymbol{u}^h = \sum_{j=1}^{n} N_j \delta \mathbf{d}_j, \quad \delta T^h = \sum_{j=1}^{n} N_j \delta \mathbf{T}_j, \quad \delta \lambda_c^h = \sum_{j \in S} \phi_j \delta \boldsymbol{\Lambda}_{c,j}. \tag{20}$$

For more information on the choice of the ansatz functions ϕ_j for the Lagrange multiplier field, the interested reader is referred to [30,32]. Eventually, the semi-discrete solid mechanics problem can be obtained by substituting (19) and (20) into the weak form (2), resulting in:

$$\mathbf{M}_u \ddot{\mathbf{d}} + \mathbf{f}_u^{\mathrm{int}}(\mathbf{d}, \mathbf{T}) - \mathbf{f}_u^{\mathrm{ext}} + \mathbf{f}_u^c = \mathbf{0}, \tag{21}$$

where $\mathbf{M}_u$ represents the constant mass matrix and $\mathbf{M}_u \ddot{\mathbf{d}}$ corresponds to the nodal force vector resulting from the inertia virtual work contribution $\delta \mathcal{W}_u^{\mathrm{iner}}$, $\mathbf{f}_u^{\mathrm{int}}$ is the nodal internal force vector resulting from $\delta \mathcal{W}_u^{\mathrm{int}}$, and the nodal external force vector is denoted as $\mathbf{f}_u^{\mathrm{ext}}$ and associated with $\delta \mathcal{W}_u^{\mathrm{ext}}$. Lastly, $\mathbf{f}_u^c$ in (21) is the nodal contact force vector which is associated with the contact virtual work (14) and given as

$$\mathbf{f}_u^c = [\mathbf{0}, -\boldsymbol{M}(\mathbf{d}), \boldsymbol{D}(\mathbf{d})]^{\mathrm{T}} \boldsymbol{\Lambda}_c, \tag{22}$$

where $\boldsymbol{D}$ and $\boldsymbol{M}$ are the well-known mortar matrices [32]. Equation (22) is obtained after rearranging the global displacement vector in a set of inactive $\mathcal{I}$, master $\mathcal{M}$, and slave $\mathcal{S}$ degrees of freedom.

The spatial discretization of the mechanical problem is completed by discretizing also the contact constraints (13). The constraints are discretized using the Lagrange multiplier ansatz functions ϕ_j (19), resulting in

$$\tilde{g}_{n,j} := \int_{\gamma_c^{(1),h}} \phi_j g_n^h \, \mathrm{d}\gamma \geq 0, \quad \lambda_{c,n,j} \leq 0, \quad \lambda_{c,n,j} \tilde{g}_{n,j} = 0 \quad \forall j \in \mathcal{S} \quad \text{on} \quad \gamma_c^{(1)}, \tag{23}$$

where $\tilde{g}_{n,j}$ is referred to as weighted nodal gap and $\lambda_{c,n,j}$ is the normal component of the nodal Lagrange multiplier $\boldsymbol{\Lambda}_{c,j}$ (see [32]). To enforce the normal contact constraint (23), we employ a penalty regularization as detailed in [32]. Accordingly, the contact pressure $\lambda_{c,n}$ and weighted gap $\tilde{g}_n$ at every slave node j are related by introducing a penalty parameter $0 < \epsilon_c < \infty$ according to

$$\lambda_{c,n,j} = \epsilon_c \langle -\tilde{g}_{n,j} \rangle, \tag{24}$$

where $\langle \cdot \rangle$ denotes the Macauley bracket. As a consequence of the regularization, the nodal Lagrange multipliers are no longer primary variables. For a comprehensive treatment of penalty-regularized mortar finite element methods, the interested reader is referred to [27].

Remark 2.4.1. The choice of the penalty parameter affects the accuracy of the contact problem. To circumvent prohibitively large penetration for too low values of the penalty parameter as well as ill-conditioning for too high values of the penalty parameter, an adaptive penalty parameter scaling can be employed as shown in [31].

The semi-discrete thermal problem is achieved by substituting (19) and (20) in (3) and reads:

$$\mathbf{M}_T \dot{\mathbf{T}} + \mathbf{f}_T^{\text{int}}(\mathbf{d}, \mathbf{T}) - \mathbf{f}_T^{\text{ext}} + \mathbf{f}_T^c = \mathbf{0}, \tag{25}$$

where $\mathbf{M}_T$ is the constant heat capacity matrix, $\mathbf{f}_T^{\text{int}}$, $\mathbf{f}_T^{\text{ext}}$, and $\mathbf{f}_T^c$ are the nodal thermal internal, external, and contact forces, respectively. In (25), $\mathbf{M}_T \dot{\mathbf{T}}$, $\mathbf{f}_T^{\text{int}}$, $\mathbf{f}_T^{\text{ext}}$, and $\mathbf{f}_T^c$ result from the virtual work contributions $\delta \mathcal{W}_T^{\text{iner}}$, $\delta \mathcal{W}_T^{\text{int}}$, $\delta \mathcal{W}_T^{\text{ext}}$, and $\delta \mathcal{W}_T^c$, respectively. For simplicity, the external forces ($\mathbf{f}_u^{\text{ext}}$ and $\mathbf{f}_T^{\text{ext}}$) are assumed to be independent of the displacement and temperature field.

Next, the temporal discretization of the solid dynamics problem is achieved using a generalized-α time integration scheme. The discrete solid mechanics problem for the time interval $[t^n, t^{n+1}]$ with step Δt reads

$$\mathbf{r}_u\left(\mathbf{d}^{n+1}, \mathbf{T}^{n+1}\right) = \mathbf{M}_u \ddot{\mathbf{d}}^{n+1-\alpha_{u,M}} + \mathbf{f}_u^{\text{int},n+1-\alpha_{u,f}} - \mathbf{f}_u^{\text{ext},n+1-\alpha_{u,f}} + \mathbf{f}_u^{c,n+1} = \mathbf{0}, \tag{26}$$

where the superscript $n + 1 - \alpha_{u,(\cdot)}$ denotes quantities evaluated at generalized mid-points within the time interval $[t^n, t^{n+1}]$ based on generalized-α parameters $\alpha_{u,(\cdot)}$ (see, e.g., [30,33] for more details). In (26), all terms except $\mathbf{f}_u^{\text{int},n+1-\alpha_{u,f}}$ and $\mathbf{f}_u^{c,n+1}$ are evaluated in a standard manner, i.e., the value at the generalized mid-point is obtained by linearly combining the values at t^n and t^{n+1} (see, e.g., [30,32]). In contrast, the contact force $\mathbf{f}_u^c$ is computed at t^{n+1} to avoid an undesirable violation of energy conservation in the discrete system in the event of a changing active contact surface as stated in [30]. The evaluation of the deformation gradient, elastic right Cauchy–Green tensor and stress tensor, as required to compute the nodal internal force vector $\mathbf{f}_u^{\text{int},n+1}$ from $\delta \mathcal{W}_u^{\text{int}}$, is conducted as follows: The total deformation gradient at t_{n+1} is given as

$$\boldsymbol{F}^{n+1} = \boldsymbol{F}_e^{n+1} \boldsymbol{F}_{in}^{n+1}. \tag{27}$$

To avoid numerically involved linearizations of the principal stretch directions $\boldsymbol{N}_C$, the inelastic deformation gradient $\boldsymbol{F}_{in}^{n+1}$ at t^{n+1} is approximated according to

$$\boldsymbol{F}_{in}^{n+1} = \sum_{i=1}^{3} \lambda_{in}^{i,n+1} \boldsymbol{N}_C^{i,n} \otimes \boldsymbol{N}_C^{i,n}, \tag{28}$$

where the magnitude of the inelastic expansion is found by explicit time integration of the corresponding rate equation (6) using an explicit Euler scheme, i.e., $\lambda_{in}^{i,n+1} = \lambda_{in}^{i,n} + \dot{\lambda}_{in}^{i,n} \Delta t$ with $\dot{\lambda}_{in}^{i,n} = f(T^n, \boldsymbol{S}^n, \alpha^n)$. Here, $\boldsymbol{N}_C^{i,n}$ is computed from the spectral decomposition of $\boldsymbol{C}^n$. The elastic deformation gradient results from $\boldsymbol{F}_e^{n+1} = (\boldsymbol{F}_{in}^{n+1})^{-1} \boldsymbol{F}^{n+1}$, and the right Cauchy–Green tensor is determined according to

$$\boldsymbol{C}_e^{n+1} = (\boldsymbol{F}_e^{n+1})^{\text{T}} \boldsymbol{F}_e^{n+1}. \tag{29}$$

Finally, the second Piola–Kirchhoff stress tensor is computed as

$$\boldsymbol{S}^{n+1} = 2(\boldsymbol{F}_{in}^{n+1})^{-1} \frac{\partial \Psi_e(\boldsymbol{C}_e^{n+1})}{\partial \boldsymbol{C}_e^{n+1}} (\boldsymbol{F}_{in}^{n+1})^{-\text{T}}. \tag{30}$$

In a similar fashion, the fully discrete thermal problem is achieved based on a generalized-α time integration scheme and reads

$$\mathbf{r}_T\left(\mathbf{d}^{n+1}, \mathbf{T}^{n+1}\right) = \mathbf{M}_T \dot{\mathbf{T}}^{n+\alpha_{T,M}} + \mathbf{f}_T^{\text{int},n+\alpha_{T,f}} - \mathbf{f}_T^{\text{ext},n+\alpha_{T,f}} + \mathbf{f}_T^{c,n+\alpha_{T,f}} = \mathbf{0}. \tag{31}$$

Finally, the solution of the coupled non-linear problem (26) and (31) is found in a monolithic manner using the classical Newton–Raphson method with consistent linearization. The linearized system is solved using iterative solvers based on preconditioners such as AMG(BGS) as studied in [33,34].

3. Mesh adaptation

The proposed mesh adaptation consists of two steps: mesh refitting and subsequent data transfer. In the mesh refitting step we construct a "new mesh" with improved quality compared to the "old mesh". The "old mesh" is the starting point of this procedure and usually exhibits heavily distorted elements, i.e., a low mesh quality. In the second step, the associated data, e.g., nodal primary variables and history variables of the material model defined at quadrature points, is transferred from the old mesh to the new one. These two steps are described in the following. All methods presented throughout this article are implemented in our in-house parallel multi-physics research code 4C [35].

3.1. Mesh refitting

The objective of the mesh refitting (MR) step is to achieve high-quality elements which are less distorted while preserving the topology of the boundary, i.e., the total volume of the domain. Thereto, we define an element distortion potential and solve for the minimum of this potential during the mesh refitting step, thus minimizing the distortion of the finite element mesh. As mentioned before, an additional requirement for the MR step is the preservation of the boundary topology, which requires to prohibit motion of boundary nodes in the direction normal to the boundary of the problem. However, motion of the boundary nodes should be
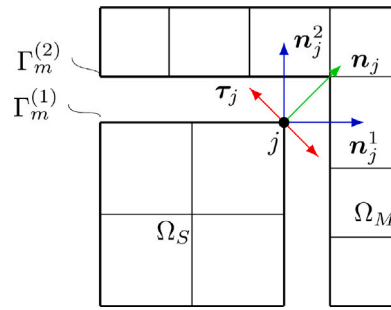
Fig. 2. Geometry with sharp edge. The slave and master bodies are denoted by Ω_S and Ω_M, respectively. The sliding surfaces of the slave and master meshes are represented by $\Gamma_m^{(1)}$ and $\Gamma_m^{(2)}$. At the corner node j, the tangent vector is $\boldsymbol{\tau}_j$, and the averaged normal vector is $\boldsymbol{n}_j$, with $\boldsymbol{n}_j^1$ and $\boldsymbol{n}_j^2$ representing the two distinct normal vectors at this node. (For interpretation of the references to color in this figure legend, the reader is referred to the web version of this article.)

permitted in tangential direction to allow for an optimal mesh relaxation also in the domains close to the boundary. This aspect is crucial for problems involving interface phenomena such as contact mechanics, which often result in a strong mesh distortion at the boundaries of the interacting bodies. These two requirements, i.e., prohibiting the normal displacement component while allowing free tangential movement for boundary nodes will be fulfilled by employing a novel mortar mesh sliding approach.

In the following, the mortar mesh sliding approach (Section 3.1.1) is presented, followed by the definition of the element distortion potential in Section 3.1.2. Finally, in Section 3.1.3, the complete description of the MR problem is given.

3.1.1. Mesh sliding approach

Mesh sliding denotes a relative motion at the interface of two meshes that allows for free tangential sliding without detachment. To formulate such a constraint, the two bodies in Fig. 1 shall be considered, which are initially in contact. To enforce non-detachment, the normal gap has to remain zero during the motion, i.e.,

$$g_n = 0. \tag{32}$$

Since no resistance with respect to tangential relative motion shall be applied, the tangential component of the interface traction vector has to vanish, similar to the friction-less contact scenario discussed before:

$$t_\tau \cdot \boldsymbol{\tau} = 0. \tag{33}$$

Identical to the mechanical contact case in Section 2.3, the contribution of the mesh sliding constraint to the virtual work of the mesh refitting problem in terms of the Lagrange multiplier λ_m can be written as:

$$\delta \mathcal{W}_u = -\int_{\gamma_c^{(1)}} [\![\delta \boldsymbol{u}]\!] \cdot \lambda_m \, \mathrm{d}\gamma = \int_{\gamma_c^{(1)}} \delta g_n \lambda_{m,n} \, \mathrm{d}\gamma = 0, \tag{34}$$

where the normal component of the Lagrange multiplier is $\lambda_{m,n} = \lambda_m \cdot \boldsymbol{n}$. Following the mortar finite element formulation presented above, the spatially discretized mesh sliding force vector $\mathbf{f}_u^m$ is identical to the vector $\mathbf{f}_u^c$ in (22). The only difference between the mesh sliding approach and the friction-less contact case presented above is given through the constraints (13) and (32), where the former represents an inequality constraint and the latter an equality constraint. Keeping this difference in mind, the mesh sliding constraints are enforced through a regularization based on the discretized weighted nodal gap $\tilde{g}_{n,j}$ (see (23)) and a penalty parameter $0 < \epsilon_m < \infty$, which yields for node j:

$$\lambda_{m,n,j} = \lambda_{m,j} \cdot \boldsymbol{n}_j = -\epsilon_m \tilde{g}_{n,j}, \quad \lambda_{m,j} \cdot \boldsymbol{\tau}_j = 0 \quad \forall j \in S. \tag{35}$$

The significant difference between the penalty regularization of the mesh sliding (35) and the mechanical contact (24) is the Macaulay brackets. They must be used in contact mechanics because contact forces only exist if the gap is negative. In contrast, in mesh sliding, the forces exist regardless of the sign of the gap to prevent penetration and detachment.

Remark 3.1.1. We employ mesh sliding to allow free tangential sliding on relatively smooth surfaces to minimize mesh distortions close to the interface. However, due to the construction of the mesh sliding constraints, it is inherent to the method that sharp edges or corners in the mesh sliding interface can lead to a penetration of the bodies at this interface. To explain this issue, we consider a square body Ω_S with a corner node j and an L-shaped body Ω_M as shown in Fig. 2. As it is not straightforward to define the normal at a corner node since the normals of the adjacent edges are not parallel $(\boldsymbol{n}_j^1, \boldsymbol{n}_j^2)$, we apply a common strategy from computational contact mechanics, i.e. we construct an averaged normal $(\boldsymbol{n}_j)$ at the corner. The averaged normal $(\boldsymbol{n}_j)$ at the corner j points along the diagonal of the square (green vector), and the tangential vector (red vector) are constructed as shown in Fig. 2. According to the definition of the mesh sliding constraint, the nodes are free to move in the tangent plane. As a consequence, the node j can penetrate into Ω_M, keeping the gap zero in a weighted sense, i.e., $\tilde{g}_{n,j} = 0$.

In this work for the numerical examples showcased in Section 4, the discussed phenomenon is avoided by applying a displacement Dirichlet boundary condition $\boldsymbol{u} = \boldsymbol{0}$ (equivalent to mesh tying) to the slave and master nodes of sharp corners or edges. As a result, there is no relative motion between the slave and master side.
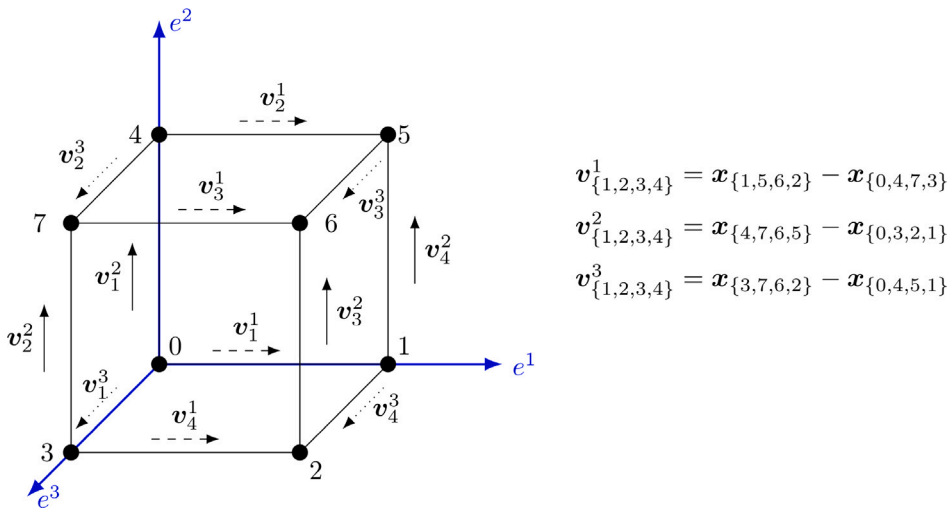
Fig. 3. Illustration of edge vectors defined to formulate included angle and edge constraints for a hexahedral element.

$$v^1_{\{1,2,3,4\}} = x_{\{1,5,6,2\}} - x_{\{0,4,7,3\}}$$
$$v^2_{\{1,2,3,4\}} = x_{\{4,7,6,5\}} - x_{\{0,3,2,1\}}$$
$$v^3_{\{1,2,3,4\}} = x_{\{3,7,6,2\}} - x_{\{0,4,5,1\}}$$

3.1.2. Element distortion potential

Generally, mesh quality can be measured in geometric quantities such as skewness and aspect ratio. The skewness quantifies the angles enclosed by the element faces or edges, whereas the aspect ratio measures the ratio of the dimensions of elements in different spatial directions. In this work, we control the element size and aspect ratio by enforcing constraints on the element edge lengths, denoted as G_E, and the skewness by enforcing constraints on the angles enclosed by the element edges, denoted as G_A.

Remark 3.1.2. It is known that certain finite element formulations are sensitive to specific element distortions (e.g. trapezoidal vs parallelogram). In such cases, it is straightforward to include this knowledge in the definition of the element distortion potential.

We demonstrate the formulation of these constraints using an 8-noded hexahedral element, which is the finite element type employed in the numerical examples of this work. As shown in Fig. 3, we first define 12 edge vectors v^i_j. Here, the superscript $i \in \{1, 2, 3\}$ denotes the direction e^i associated with the orientation of the edge in parameter space. The subscript $j \in \{1, 2, 3, 4\}$ represents a counting index for the four individual edge vectors pointing to a given direction i. As illustrated in Fig. 3, each edge vector is defined as the difference vector between the (current) spatial position vectors of the two nodes associated with the edge vector. From these individual edge vectors, an averaged edge vector $\bar{v}^i$ is defined as

$$\bar{v}^i = \frac{1}{4} \sum_{j=1}^{4} v^i_j. \tag{36}$$

Based on these definitions, the edge and angle constraints will be formulated in the following.

Edge constraints G^i_E

To impose specific edge lengths on elements, we apply constraints on both, the average edge vectors $\bar{v}^i$ and the individual edge vectors v^i_j, which are denoted as $\bar{G}^i_E$ and $\hat{G}^i_E$, respectively. The constraint $\bar{G}^i_E$ on the average edge vector in direction e^i is defined as

$$\bar{G}^i_E = \frac{\sqrt{\bar{v}^i \cdot \bar{v}^i}}{l^i_r} - 1 \overset{!}{=} 0 \quad \text{for} \quad i = 1, 2, 3, \tag{37}$$

with l^i_r denoting a target element edge length in direction e^i to be prescribed. This constraint enforces the length l^i_r on the average edge vector $\bar{v}^i$. In a next step, the constraint $\hat{G}^i_E$ is defined according to

$$\left(\hat{G}^i_E\right)_j = \frac{v^i_j \cdot v^i_j}{\bar{v}^i \cdot \bar{v}^i} - 1 \overset{!}{=} 0 \quad \text{for} \quad i = 1, 2, 3, \quad j = 1, 2, 3, 4, \tag{38}$$

which enforces that each individual edge vector equals the associated average edge vector. Prescribing a spatial distribution function for the element size will be called *mesh localization* throughout this work. It can be achieved by prescribing spatial functions for the target lengths, i.e., $l^i_r = l^i_r(X)$. To sum up, so far we have defined 15 constraints associated with element size and aspect ratio, 3 on the average edge vectors and 12 on the individual edge vectors.

Angle constraints G^{mn}_A

Next, we construct angle constraints considering the angle enclosed by a pair of edge vectors v^i_j with shared node. For example, the angle constraints G^{mn}_A for node "0" are formulated as (c.f. Fig. 3)

$$G_A^{12} = \frac{\boldsymbol{v}_1^1 \cdot \boldsymbol{v}_1^2}{\|\boldsymbol{v}_1^1\|\|\boldsymbol{v}_1^2\|} - \cos\theta_r^{12} \overset{!}{=} 0,$$

$$G_A^{13} = \frac{\boldsymbol{v}_1^1 \cdot \boldsymbol{v}_1^3}{\|\boldsymbol{v}_1^1\|\|\boldsymbol{v}_1^3\|} - \cos\theta_r^{13} \overset{!}{=} 0, \qquad (39)$$

$$G_A^{23} = \frac{\boldsymbol{v}_1^2 \cdot \boldsymbol{v}_1^3}{\|\boldsymbol{v}_1^2\|\|\boldsymbol{v}_1^3\|} - \cos\theta_r^{23} \overset{!}{=} 0,$$

where θ_r^{12}, θ_r^{13}, and θ_r^{23} are the enclosed target angles to be achieved. To achieve perpendicular edges, we set $\theta_r^{12} = \theta_r^{13} = \theta_r^{23} = \pi/2$. Likewise, angle constraints can be formulated for all remaining nodes. To conclude, we have formulated 24 angular constraints in (i.e., three constraints for each of the eight nodes).

Constraint enforcement

Finally, we enforce these constraints on basis of a distortion potential with penalty parameters $\bar{\varepsilon}_E$, $\hat{\varepsilon}_E$ and ε_A given as

$$\pi_d = \frac{1}{2}\bar{\varepsilon}_E \sum_{i=1}^{ndir} \bar{G}_E^i \bar{G}_E^i + \frac{1}{2}\hat{\varepsilon}_E \sum_{i=1}^{ndir}\sum_{j=1}^{4} (\hat{G}_E^i)_j (\hat{G}_E^i)_j + \frac{1}{2}\varepsilon_A \sum_{n=1}^{nnode} (G_A^{12}G_A^{12} + G_A^{13}G_A^{13} + G_A^{23}G_A^{23})_n, \qquad (40)$$

where $ndir = 3$ is the number of spatial directions and $nnode = 8$ is the number of nodes. In the following, the meaning of the different constraint contributions shall be briefly discussed. Clearly, the constraints $\hat{G}_E^i$ penalize deviations of the individual edge lengths from the average edge length in a given direction, i.e., they enforce the element shape to equal a parallelepiped in the limit of $\hat{\varepsilon}_E \to \infty$. If additionally also the angular constraints G_A with target angles $\theta_r^{12} = \theta_r^{13} = \theta_r^{23} = \pi/2$ are enforced, the element will tend towards a cuboid shape. Eventually, if equal target lengths are chosen for the constraints $\bar{G}_E^i$, i.e., $l_r^1 = l_r^2 = l_r^3 =: l_r$, the element will approach a cubic shape. Finally, the absolute value of l_r determines how a shape-preserving scaling of the element size will be penalized. For example, by choosing l_r as the initial edge length of a regular mesh with cubic elements, every (even shape-preserving) deviation from the initial element size will be penalized. Clearly, the chosen set of $15 + 24$ constraints per element is redundant, since an hexahedral element with 8 nodes only exhibits 24 degrees of freedom (including 6 rigid body modes changing neither the shape nor the size of the element). However, this over-constraining is no problem when employing a penalty potential for constraint enforcement. Moreover, this specific choice of (redundant) constraints allows to independently control different modes of element distortion (with different effect on the mesh quality), as elaborated above. In addition, the chosen set of constraints leads to a distortion potential that is symmetric with respect to the node numbering, i.e., the result will not change if the node numbering is changed for a given mesh. In conclusion, it is emphasized that the definition of an element distortion potential is not unique. The specific choice presented above has proven effective in the numerical test cases we have investigated so far. In particular, the specification $\bar{\varepsilon}_E = \hat{\varepsilon}_E =: \varepsilon_A$ turned out as a robust choice and will be used in the remainder of this work.

Demonstration example: Effect of target element edge lengths

To conclude this section, the effect of the element constraints shall be demonstrated using the numerical example shown in Fig. 4. Consider the truncated rectangular pyramid-shaped body in Fig. 4a meshed with 42 hexahedral elements. The body is freely supported in the first quadrant, so that rigid body modes are suppressed. We solve the constraint equations (40) (see next section, for details of the solution procedure) with equal target lengths (see (37)) in all directions, i.e. $l_r^1 = l_r^2 = l_r^3$ and $\theta_r^{mn} = \pi/2$. The resulting geometry is shown in Fig. 4b. As expected the obtained geometry is rectangular with cubic elements. When $l_r^1 \neq l_r^2 \neq l_r^3$ and $\theta_r^{mn} = \pi/2$ the resulting geometry remains rectangular and contains rectangular elements as illustrated in Fig. 4c. This shows that the suggested approach is suitable to obtain elements of a specific desired shape. It is emphasized that this example has been designed to visualize the isolated effect of the element distortion potential without imposing mesh sliding constraints at the boundaries. Thus, in contrast to actual mesh refitting problems, the mesh in this demonstration example is not required to preserve the boundary contour of the discretized body.

3.1.3. Problem description of mesh refitting method

Let the old mesh be defined on the domain $\Omega_m \subset \Omega_t$ with boundary $\Gamma_m^{(1)} := \partial\Omega_m$. We apply the mesh sliding approach from above (see Section 3.1.1) to preserve the boundary contour of a given body while allowing for tangential sliding. This will be done only for the boundary nodes without prescribed Dirichlet boundary condition, i.e., only for nodes on the boundary $\Gamma_m^{(1)} \setminus \Gamma_u$. From a technical point of view, to enable the mesh sliding approach in the same sense as typical for mortar interface problems, we replicate the discretized boundary $\Gamma_m^{(1)}$ and denote this auxiliary boundary as $\Gamma_m^{(2)}$ (see Fig. 5). Since $\Gamma_m^{(2)}$ and $\Gamma_m^{(1)}$ coincide, a one-to-one mapping between the nodes on these boundaries exists, i.e., nodal positions can be transferred in a straight-forward manner from $\Gamma_m^{(1)}$ to $\Gamma_m^{(2)}$. It is emphasized that the auxiliary boundary $\Gamma_m^{(2)}$ is only required to represent a fictitious interaction partner to apply the standard mesh-sliding method to the boundary nodes of the original mesh on $\Gamma_m^{(1)}$. This means, that the nodal position and displacement values on the auxiliary boundary $\Gamma_m^{(2)}$ remain fixed, i.e., are prescribed per Dirichlet boundary condition, and the mesh-refitting problem does not need to be solved for these nodes.

Remark 3.1.3. To prevent changes in the topology of the body, the movement of the corner nodes must be avoided during mesh refitting. In this work, it is achieved by applying a displacement Dirichlet boundary condition $\boldsymbol{u} = \boldsymbol{0}$.
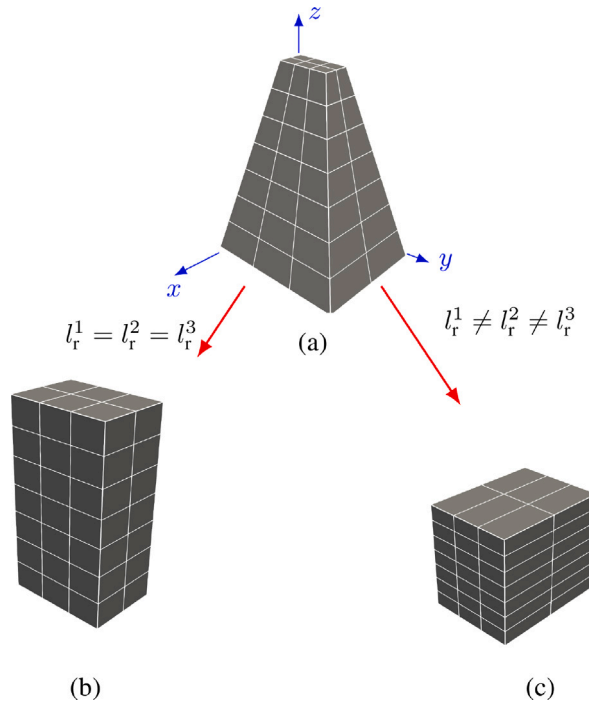
Fig. 4. Illustration of constraints: (a) initial geometry (b) resulting geometry when elemental constraints with $l_r^1 = l_r^2 = l_r^3$ and $\theta_r^{mn} = \pi/2$ are applied on (a), and (b) when $l_r^1 \neq l_r^2 \neq l_r^3$ with $\theta_r^{mn} = \pi/2$ are applied on (a).
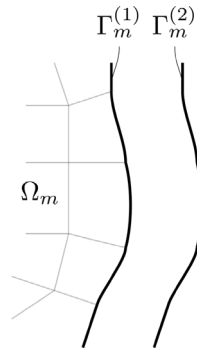

**Fig. 5.** Illustration of mesh sliding interface surfaces with auxiliary boundary $\Gamma_m^{(2)}$.

The complete MR problem is performed after solving the fully discretized thermo-mechanical problem for time step t^{n+1}, as described in Section 2.1. The solution of the mesh refitting problem is defined as the stationary value of the following total potential

$$\pi_d + \pi_m \rightarrow \text{stat.,} \tag{41}$$

where the element distortion potential π_d is given in (40) and π_m represents an abstract potential for mesh sliding constraint enforcement (e.g., a Lagrange multiplier or a penalty potential; the latter approach is used in the examples presented in the following) whose variation is given by the discretized form of (34). Similar to the weak form of our physical (thermo-mechanical) problem, as necessary condition for a stationary value the variation of the discrete potential (41) has to vanish, leading to the following system of nonlinear (residual) equations:

$$\mathbf{f}_u^d + \mathbf{f}_u^m = \mathbf{0}, \tag{42}$$

where $\mathbf{f}_u^d = \frac{\partial \pi_m}{\partial \mathbf{d}}$ is the gradient of the discrete element distortion potential (40) and $\mathbf{f}_u^m$ is the nodal mesh sliding force vector according to Section 3.1.1 (see Appendix A for more details). The solution of the non-linear system (42) is found using a Newton–Raphson scheme based on a consistent linearization.
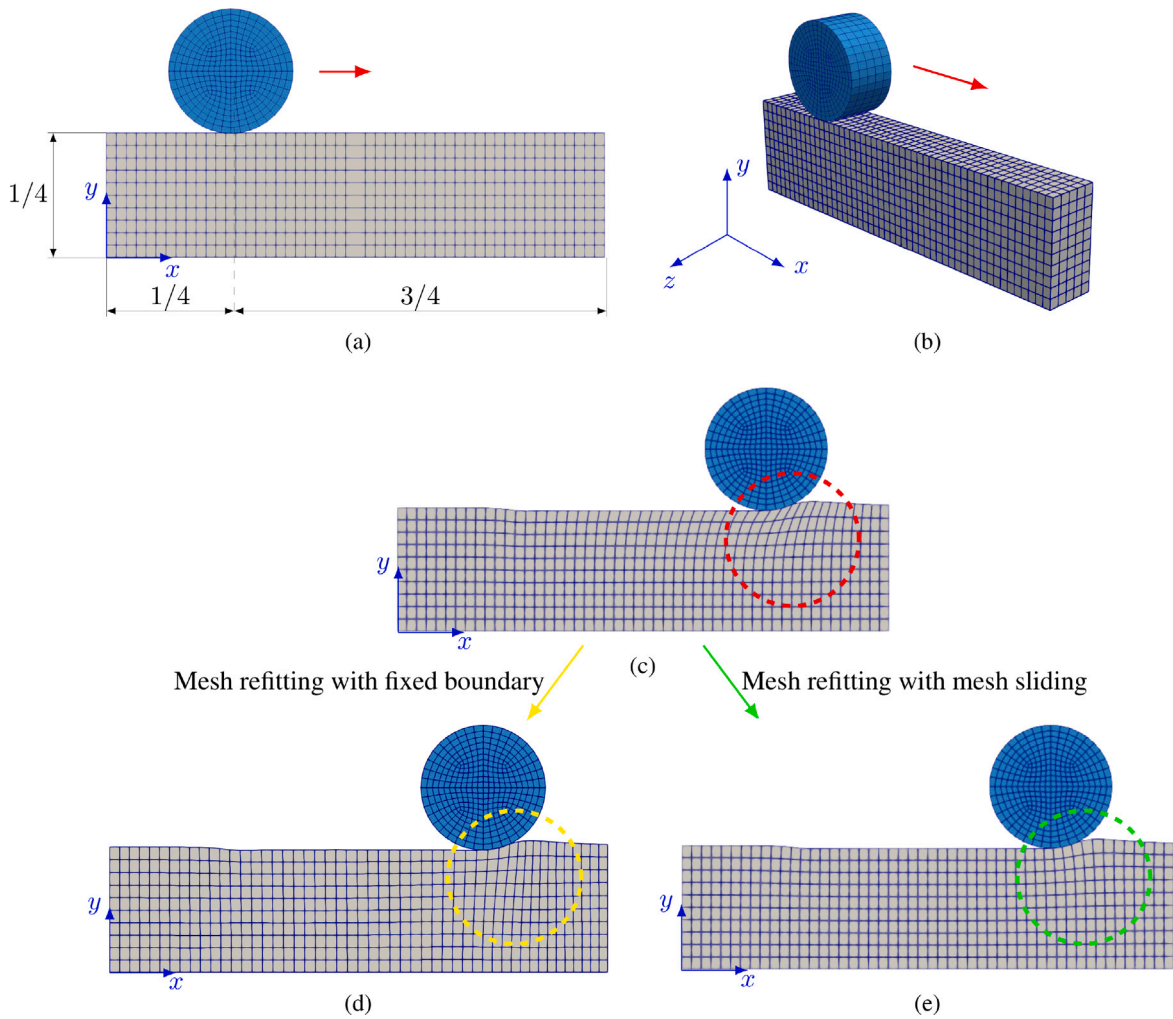
Fig. 6. Frictional sliding of a rigid cylinder with a diameter of 0.25 over a rectangular block of dimensions $1 \times 0.25 \times 0.125$: (a) and (b) show the initial configuration. (c) illustrates the final deformed state without mesh refitting. (d) shows mesh refitting with fixed boundaries for the deformed state in (c). (e) presents mesh refitting with mesh sliding for the deformed state in (c).

Remark 3.1.4. It should be noted that sometimes it is useful to execute an "artificial time step" after mesh adaptation (i.e. after mesh refitting and data transfer) to rebuild the dynamic equilibrium.

Remark 3.1.5. In this work, the reference configuration of the MR problem is updated with the (converged) current configuration of the old mesh. This means that the current state of the old mesh becomes the reference state of the MR problem. By updating the reference configuration of the MR problem with the current configuration of the old mesh the MR procedure gets more robust because the MR problem is thereby independent of the original reference configuration.

Demonstration example: Influence of mesh sliding approach

Next, we demonstrate the benefits arising from the use of the mesh sliding algorithm compared to keeping boundary nodes fixed using two numerical examples in Figs. 6 and 7. These examples are provided for illustration and a better understanding of these specific effects only and are not designed to demonstrate the extreme cases that our approach can handle. First, consider the isothermal frictional sliding of a rigid cylinder over a rectangular block as shown in Fig. 6. The rigid cylinder has a diameter of 0.25 with height 0.125, and the rectangular block has the dimensions $1 \times 0.25 \times 0.125$ (see Figs. 6(a) and 6(b)). The rectangular block is meshed with 2500 cubic 8-noded hexahedral elements and is modeled with a finite strain hyperelastoplastic material model as studied in Section 3.4.2.5 of [36]. The isothermal frictional contact is modeled using the mortar penalty method presented in [37]. The motion of the cylinder is completely displacement-controlled. First, the cylinder is pressed onto the rectangular block by displacing the cylinder through 0.005 in the $-y$ direction. Next, the cylinder is moved from $x = 0.25$ to $x = 0.75$ in a straight
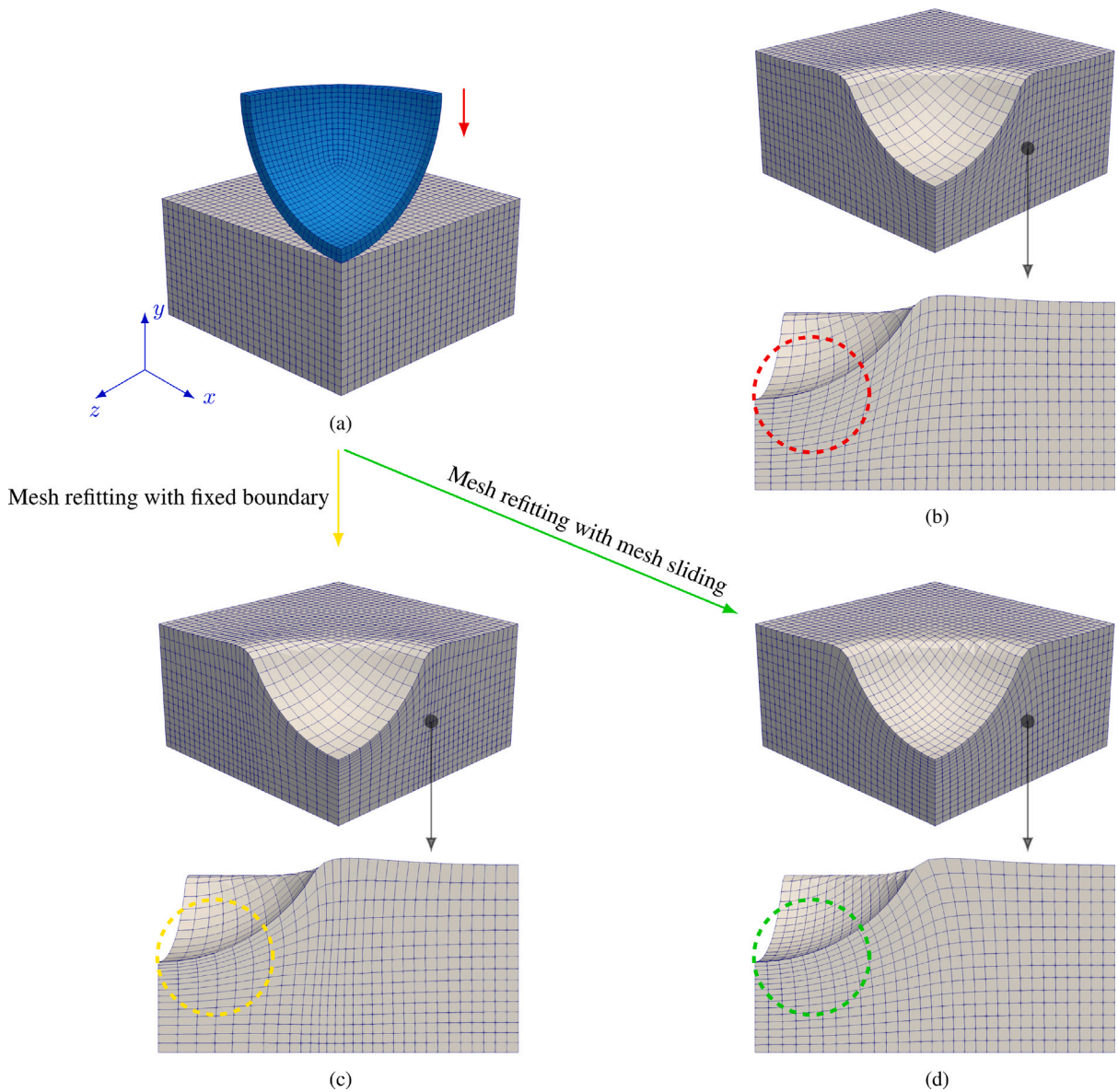
Fig. 7. Elasto-plastic punching of a rectangular block of dimensions $0.5 \times 0.5 \times 0.25$ by a rigid sphere of outer radius 0.25: (a) reference configuration. (b) final deformed state without mesh refitting. (c) The solution of the same physical problem with accompanying mesh refitting after every time step with mesh sliding and (d) with fixed boundary, respectively. In the subfigures (b)–(d), the rigid sphere is hidden to provide a clear view of the deformed zone. (For interpretation of the references to color in this figure legend, the reader is referred to the web version of this article.)

line. This procedure induces elastic and plastic deformation on the top surface of the block as shown in Fig. 6(c). It can be seen that the boundary elements underneath the cylinder (shown in a red dashed circle) have experienced shear distortion and this boundary is under consideration for mesh sliding. At this deformed state, the presented mesh refitting is performed with fixed boundary and mesh sliding and the resulting new mesh configurations are illustrated in Figs. 6(d) and 6(e). When MR is performed with a fixed boundary, the original cubic shape of the elements cannot be restored, as is evident from the elements within the yellow dashed circle in Fig. 6(d). However, in MR with mesh sliding (see Fig. 6(e)), the refitted mesh in the whole domain, and in particular in the region below the cylinder (shown in a green dashed circle), resembles the initial uniform mesh, i.e., cubic elements. This is achieved by the free tangential sliding of the boundary nodes in the mesh refitting step. In short, in case of pure shear at the boundary, the quality of the refitted mesh is close to the initial mesh after applying the mesh sliding approach.

The second example investigates the punching of a rectangular block by a rigid sphere. Only a quarter part is modeled exploiting the symmetry of the problem configuration (see Fig. 7(a)). The quarter rectangular block of size $0.5 \times 0.5 \times 0.25$ is modeled with a hyperelastoplastic model, the same as in the first example, and meshed with 13500 cubic 8-noded hexahedral elements. The rigid

quarter sphere has an outer radius of 0.25 and is represented by the blue colored body in Fig. 7(a). Isothermal frictionless contact is applied as presented in Section 2.3. The sphere segment is moved vertically downwards by a distance equal to half of the block thickness, i.e., 0.125, in 125 load steps. This induces elastic and plastic deformations in the rectangular block as depicted in Fig. 7(b). The elements near the upper surface of the block are largely distorted, especially in the transition region between the contact and non-contact areas (highlighted by the red dashed circle in Fig. 7(b)). This boundary is considered for mesh sliding. Mesh refitting was carried out at every time step using two different variants, one with fixed boundary and one with mesh sliding. In MR with mesh sliding, as shown in the Fig. 7(c), mesh contains less distorted elements at the boundary and inside the volume. Furthermore, the contact area has more elements than the original problem. Moreover, the gradual transition of element shape from the boundary to the volume, as highlighted in the green dashed circle in Fig. 7(c), shows a significant improvement. MR with fixed boundary nodes can lead to a strong mesh distortion in the boundary region, which can in turn deteriorate the convergence of nonlinear solvers. In this example, convergence using the Newton–Raphson scheme could not be achieved with the same number of load steps when boundary nodes were fixed. Instead, the number of load steps had to be increased to 250, i.e., doubled, to achieve convergence. In addition, even the penalty parameters for MR had to be reduced. The resulting mesh, illustrated in Fig. 7(d), reveals that the quality of the mesh at the boundary does not show significant improvement when compared to MR with mesh sliding, as evident in the yellow dashed circle.

For both shown examples, no significant improvement of the mesh quality could be achieved if the boundary nodes where kept fixed. Thus, mesh sliding is required to obtain a proper mesh relaxation also in boundary regions, especially for problems with large boundary distortion.

3.1.4. Algorithmic aspects of the mesh refitting method

In the following, more detailed algorithmic aspects of the overall mesh refitting approach will be presented.

Target shape incrementation scheme

The non-linear problem in (42) may not be solvable in one step if the old mesh is heavily distorted. To improve convergence of the Newton–Raphson scheme we employ an incrementation approach to the target lengths in (37) and target angles in (39). Thereto, we define N incrementation steps for the mesh refitting algorithm during which the incrementation factor $\alpha_{n_{inc}} \in [0, 1]$, with $n_{inc} \in 1, \ldots, N$, is increased from 0 to 1. Let l^i_{e0} and θ^{ij}_{e0} be the element average lengths and angles of the original distorted mesh at the beginning of the MR algorithm (updated reference configuration). Moreover, l^i_r and θ^{ij}_r are the target element edge lengths and angles to achieve. Then, for the current incrementation step n_{inc}, the elemental target lengths and angles are defined as

$$\left(l^i_r \right)_{n_{inc}} = l^i_{e0} + \alpha_{n_{inc}} \left(l^i_r - l^i_{e0} \right), \tag{43}$$

$$\left(\theta^{ij}_r \right)_{n_{inc}} = \theta^{ij}_{e0} + \alpha_{n_{inc}} \left(\theta^{ij}_r - \theta^{ij}_{e0} \right). \tag{44}$$

For the numerical examples considered in this work, the target angles are set to $\theta^{ij}_r = \pi/2$.

Remark 3.1.6. The target incrementation scheme is similar to a classical substepping procedure. When a Newton step is not converged the step size is subdivided. However, when a prescribed number of consecutive sub-steps converges in a few iterations, the sub-step size can be increased again.

Uniform mesh regularization

The aim of a purely uniform mesh regularization is to achieve uniform element sizes and shapes inside the entire problem domain. To achieve this goal, we prescribe the target element edge lengths as the average element edge length within the total problem domain determined for the (original) distorted mesh. The average edge length $\bar{l}^i_r$ is defined as

$$\bar{l}^i_r = \frac{1}{N_e} \sum_{j}^{N_e} \|(\bar{\boldsymbol{v}}^i)_j\|, \tag{45}$$

where N_e is the number of elements in Ω_m and the index i refers to the direction e^i in parameter space.

Mesh localization

To achieve different target element edge lengths at different locations of the problem domain, we define a continuous spatial distribution function for l^i_r:

$$l^i_r(\boldsymbol{X}) = l^i_{r0} f(\boldsymbol{X}), \tag{46}$$

where $f(\boldsymbol{X})$ is a spatial function and l^i_{r0} is a reference value of the target element edge length; for instance, it can be an average length as defined in (45). In this work, we employ the following exponential function:

$$f(\boldsymbol{X}) = 1 + \exp\left(-c\|\boldsymbol{X} - \boldsymbol{X}_0\|^2\right), \tag{47}$$

where the parameter c controls the rate of decay of the function when departing from the reference point $\boldsymbol{X}_0$. According to (47), the distribution function $l^i_r(\boldsymbol{X})$ reproduces the reference value l^i_{r0} when evaluated at the reference point $\boldsymbol{X}_0$. In practice, the reference point $\boldsymbol{X}_0$ typically represents a location of the physical problem, which is characterized by strong gradients of the primary variables accompanied by a significant mesh distortion. Thus, the mesh localization approach allows to have smaller elements, i.e., a higher mesh resolution, at this location. Moreover, to enforce a high mesh quality, i.e., small element distortions, at this critical location, also the penalty parameters may be prescribed as spatial functions based on (47), i.e., $\varepsilon_E(\boldsymbol{X}) = \varepsilon_{E0} f(\boldsymbol{X})$ and $\varepsilon_A(\boldsymbol{X}) = \varepsilon_{A0} f(\boldsymbol{X})$.

$$l_r^i = \bar{l}_r^i \qquad\qquad\qquad\qquad\qquad\qquad\qquad l_r^i = l_{r0}^i \left(1 + \exp\left(-c \parallel \boldsymbol{X} - \boldsymbol{X}_0 \parallel^2\right)\right)$$

(a)

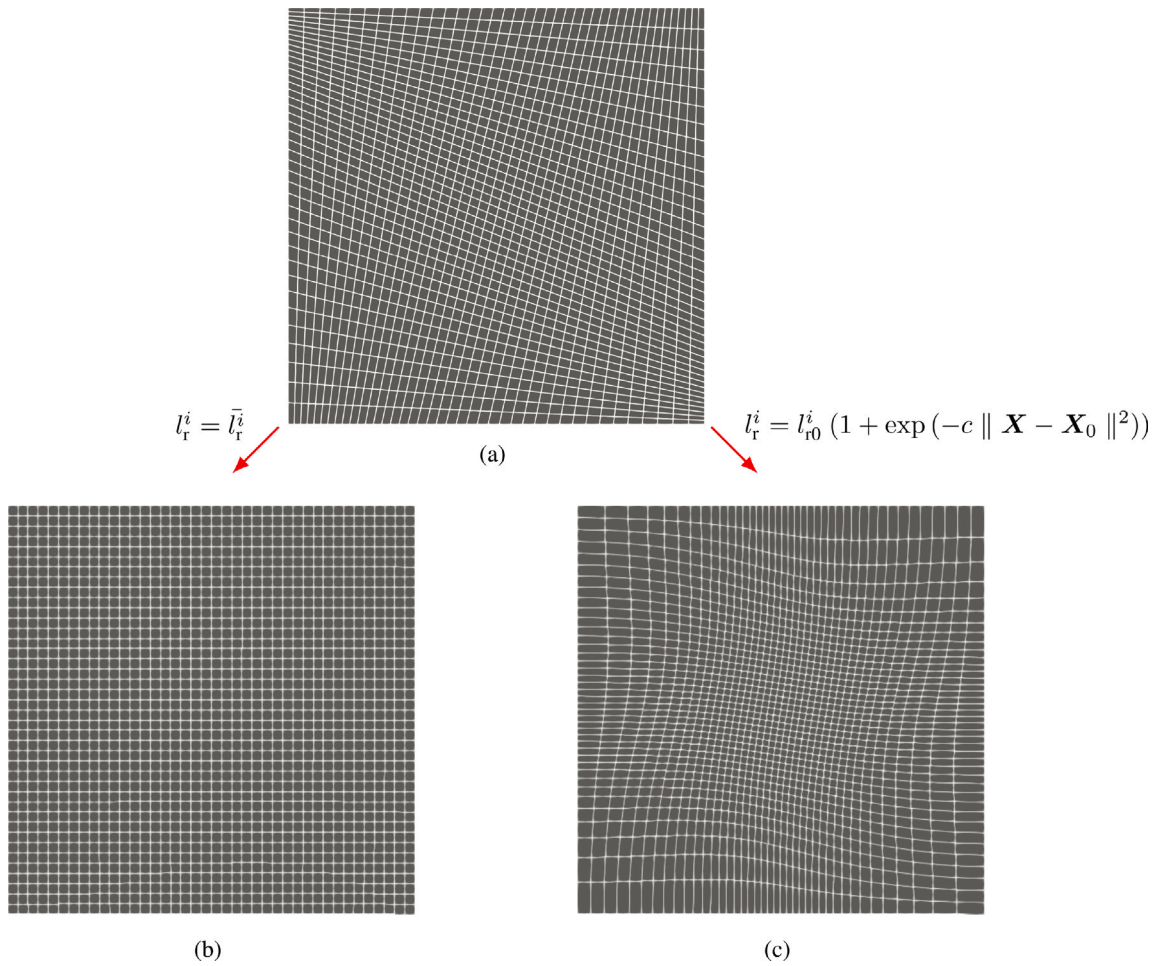(b)   (c)

Fig. 8A. Illustration of mesh regularization and localization: (a) an initial distorted mesh. (b) and (c) show uniformly regularized and localized meshes, with smaller elements at the center of the square, both with $\bar{\varepsilon}_E = \hat{\varepsilon}_E = \varepsilon_A = 0.01$.

Demonstration example: Uniform mesh regularization and localization

Uniform mesh regularization and localization shall be illustrated by a 2-dimensional numerical example defined on a 2×2 domain. The initial distorted mesh is created by 40 unequal divisions of the edges resulting in 1600 elements as illustrated in Fig. 8A(a). To achieve a uniform regularized mesh, we set the target lengths to an average length according to (45). The resulting meshes for different penalty parameter combinations are shown in Figs. 8A(b), 8B(d), and 8B(f), which clearly confirm the underlying idea of the uniform mesh regularization approach. However, it can be observed that, irrespective of the choice of the penalty parameters, the exact solution, i.e., cuboid shapes, is recovered. On the other hand, a localization is achieved using an exponential function according to (47) with $l_{r0}^i = 0.025$, $c = 0.1$, and $\boldsymbol{X}_0$ representing the center of the domain. The resulting mesh for different penalty parameter combinations are portrayed in Figs. 8A(c), 8B(e) and 8B(g). As desired, this approach allows to achieve a higher mesh resolution with very regular elements at the location of interest, i.e., the center of the domain. Of course, this ansatz compromises the mesh quality in other regions of the problem setup. Nevertheless, it can be very helpful in scenarios with very strict requirements on the mesh quality in certain regions of the problem.

In the latter case of mesh localization, the choice of the penalty parameters will influence the mesh quality after refitting. The relative weights will determine the strictness of enforcing the corresponding constraint. For example, on the one hand, a higher $\bar{\varepsilon}_E$ or $\hat{\varepsilon}_E$ will prioritize controlling the aspect ratio of the mesh over skewness. This is why, in Fig. 8B(e), the angular constraint is less pronounced in comparison to Fig. 8B(g). On the other hand, a higher ε_A will result in the strict enforcement of the angular constraint G_A, producing a mesh with lower skewness. This, in combination with mesh localization (discussed in Section 3.1.4), provides the flexibility to adapt the method to the problem requirements.
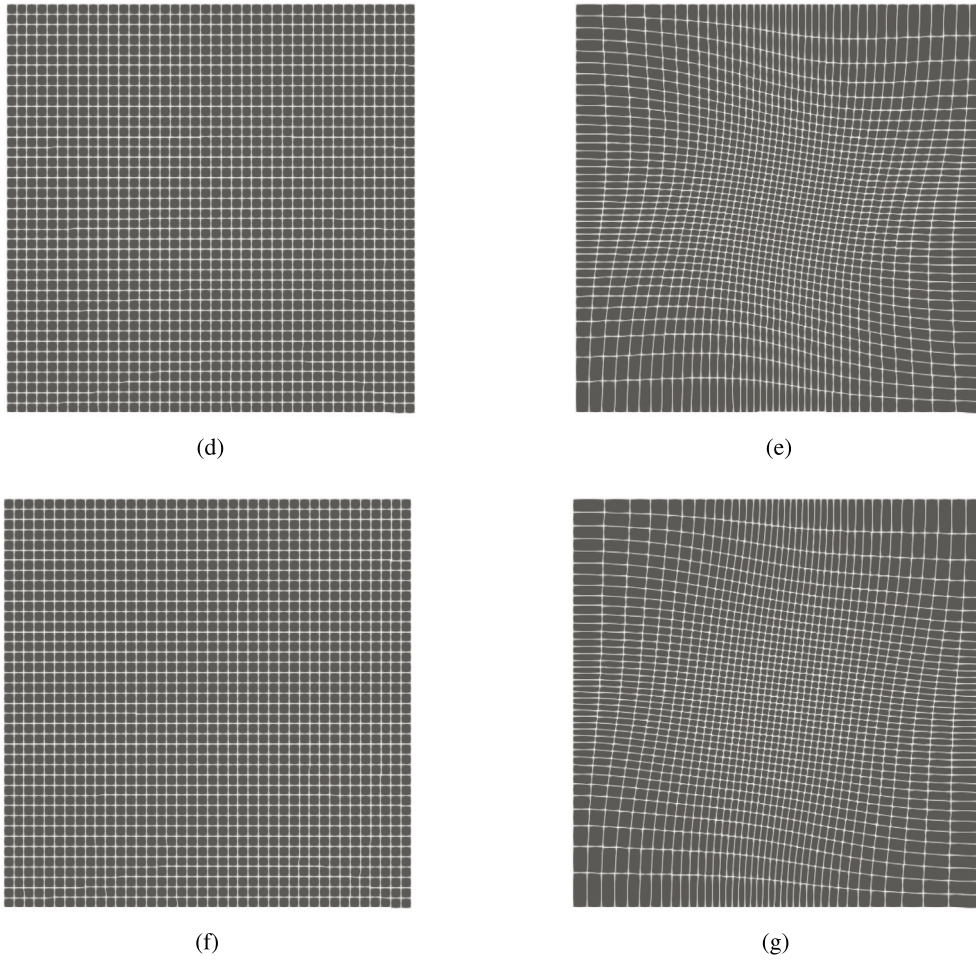
(d)

(e)

(f)

(g)

Fig. 8B. Illustration of mesh regularization and localization continued from Fig. 8A: (d) and (e) present uniformly regularized and localized meshes, again with smaller elements at the center, with $\bar{\varepsilon}_E = \hat{\varepsilon}_E = 0.015$ and $\varepsilon_A = 0.001$. (f) and (g) show similar meshes, but with $\bar{\varepsilon}_E = \hat{\varepsilon}_E = 0.001$ and $\varepsilon_A = 0.03$.
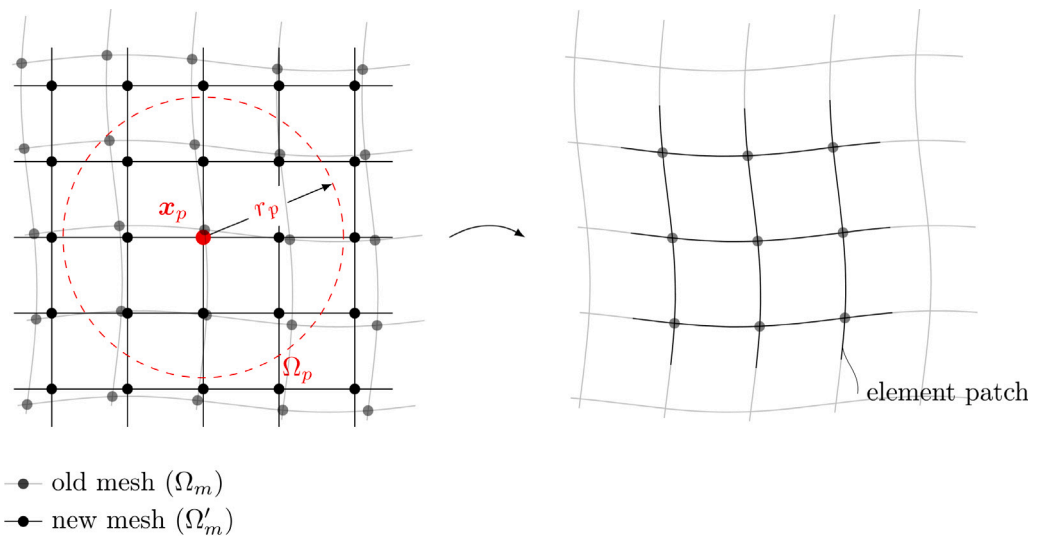

Fig. 9. Illustration of element patch for transferring data from old mesh to new mesh.

3.2. Transfer of mesh data

Within our overall mesh refitting approach, the transfer of data from the old (distorted) mesh on Ω_m to the new (regularized) mesh on Ω'_m is a critical aspect. The variables to be transferred include nodal primary variables (i.e., displacement and temperature field) but also internal material variables (e.g., the inelastic deformation gradient) defined at quadrature points. These variables can be broadly classified as scalars, vectors, and tensors, whereas the latter represents the most challenging case from a data transfer point of view. This section presents the main strategy for data transfer as employed in this work including a tensor interpolation scheme proposed in our recent contribution [22]. It is emphasized that the proposed data transfer schemes are independent of the mesh refitting scheme proposed in the previous sections, and can be combined with arbitrary mesh regularization, mesh refinement and remeshing schemes.

Consider an element node or quadrature point located at x_p in the new mesh Ω'_m. To determine the new data at x_p, we interpolate data from an element patch $\Omega_p \subset \Omega_m$ within a radius of r_p around this point (see Fig. 9). Let $x_j \in \{x_1, \ldots, x_N\}$ be a set of position vectors in Ω_p, while $\alpha_j \in \{\alpha_1, \ldots, \alpha_N\}$ and $T_j \in \{T_1, \ldots, T_N\}$ represent scalar- and tensor-valued data associated with these points. The methods presented in the following rely on a relative weighting of data considering the distance of the data points from the interpolation point. For this purpose, we employ the normalized weighting function $\bar{w}(x_j)$ according to:

$$\bar{w}(x_j) := \frac{w(x_j)}{\sum_{j=1}^{N} w(x_j)} \quad \text{such that} \quad \sum_{j} \bar{w}(x_j) = 1. \tag{48}$$

Here the weighting function $w(x_j)$ can be any monotonic continuous function that decreases as it moves away from the interpolation point x_p. For example, an exponential weighting function with control parameter c reads:

$$w(x_j) = \exp\left(-c\|x_j - x_p\|^2\right). \tag{49}$$

In the following subsection, we demonstrate methods to compute scalars and tensors at x_p, denoted as α_p and T_p.

3.2.1. Scalar interpolation

We employ two different schemes for scalar interpolation, namely the moving least squares (MLS) and the logarithmic moving least squares (LOGMLS) method. Importantly, the LOGMLS scheme preserves strict positivity of strictly positive data ($\alpha_j > 0$), but, in turn, is limited to data exhibiting this property. Furthermore, both methods preserve important additional properties such as monotonicity of the data. The two schemes are briefly outlined below.

1. *Moving least squares (MLS)*: This variant employs a spatial polynomial approximation which reads

   $$\alpha(x) := p(x)a, \tag{50}$$

   where $p(x) \in \mathbb{R}^m$ is the vector of polynomial basis functions of order m, and $a \in \mathbb{R}^m$ is the corresponding vector of coefficients. The unknown coefficient vector a is obtained by minimizing the residual

   $$r = \sum_{j=1}^{N} \bar{w}(x_j)\left(p(x_j)a - \alpha_j\right)^2. \tag{51}$$

   As a prerequisite, the order of the polynomial function m must be chosen such that $m \leq N$.
2. *Logarithmic moving least squares (LOGMLS)*: This method ensures non-negative interpolation of positive quantities. It employs a moving least squares approximation of a logarithmically transformed scalar field:

   $$\alpha(x) := \exp(p(x)a). \tag{52}$$

   In this approach, the unknown vector of coefficients a is found by minimizing the residual

   $$r = \sum_{j=1}^{N} \bar{w}(x_j)\left(p(x_j)a - \ln(\alpha_j)\right)^2. \tag{53}$$

For a detailed analysis of these two methods the reader may refer to our previous work [22].

3.2.2. Tensor interpolation

We employ rotation vector-based methods for tensor interpolation proposed in our previous work [22]. These methods exploit the polar and spectral decomposition of the tensor data according to $T_j = R_j Q_j^T \Lambda_j Q_j$, where R_j, $Q_j \in \mathbb{SO}(3)$ are rotation tensors and Λ_j is the positive definite diagonal tensor containing the eigenvalues of T_j. The general strategy for tensor interpolation relies on an individual interpolation of the rotation tensors and the eigenvalues contained in Λ_j. First, the scalar eigenvalues are individually interpolated using the schemes from Section 3.2.1 to finally reconstruct Λ_p. For interpolation of the rotation tensors R_j, Q_j specific schemes are employed that preserve, among others, the objectivity of the underlying mechanical problem and are well-established, e.g., in the field of geometrically exact beam theories [38]. This step results in the interpolated rotation tensors R_p, Q_p. Finally, the interpolated tensor T_p at x_p is reconstructed according to $T_p = R_p Q_p^T \Lambda_p Q_p$.

These interpolation methods are well suited for any invertible second-order tensor. In the context of finite element discretizations for problems of nonlinear continuum mechanics, tensor-valued history often arises for material models involving, e.g., inelastic constitutive behavior [39–41] or phase change [42–44]. Generally, these methods have been proven to preserve important properties of the tensor during interpolation (e.g., positive definiteness, objectivity, etc.) and allow for higher-order spatial convergence [22].
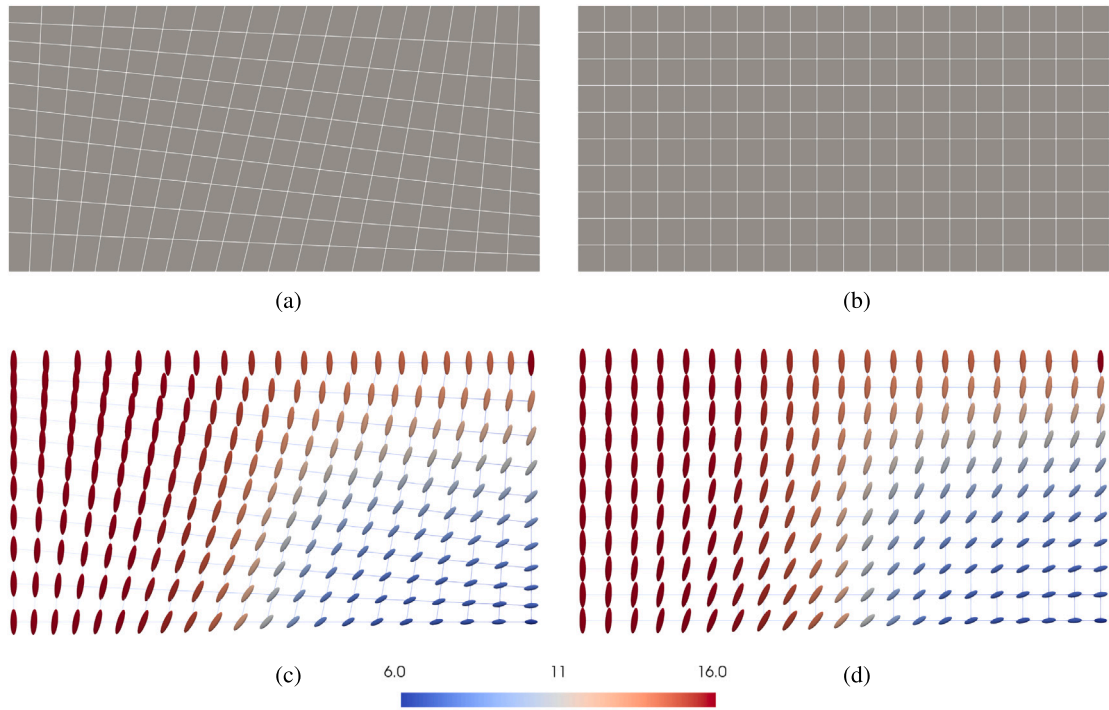
Fig. 10. Tensor interpolation example: (a) input mesh (b) regularized mesh (c) ellipsoidal representation of input tensor field (d) ellipsoidal representation of mapped tensor field. The color represents the determinant of the tensor.

Table 1
Material parameters of the expanding material.

Parameter	Value
Young's modulus (E)	1×10^4
Poisson's ratio (ν)	0
thermal conductivity (k_0)	7.55×10^6
Heat capacity (c_v)	1.4×10^{-2}

Table 2
Mesh refitting parameters.

Parameter	Value
$\bar{\varepsilon}_E, \hat{\varepsilon}_E, \varepsilon_A$	1×10^{-2}
ϵ_m	2×10^8
Maximum n_{inc}	20
Displacement tolerance	1×10^{-5}

Demonstration example: Transfer of tensor data

The tensor interpolation as part of the mesh adaptation approach is portrayed in Fig. 10. Consider an initial mesh as visualized in Fig. 10(a) with a tensor field as illustrated in Fig. 10(c) (ellipsoidal representation, see [22]). Now, the mesh regularization is performed as described in Section 3.1.3 and the resulting mesh is shown in Fig. 10(b). For tensor interpolation, we employed the "R-MLS" variant as defined in our previous work [22] to transfer tensor data from the old to the new mesh. From Figs. 10(c) and 10(d) it is evident that the method delivers a smooth interpolation while preserving the magnitude and orientation of the tensor data when mapped.
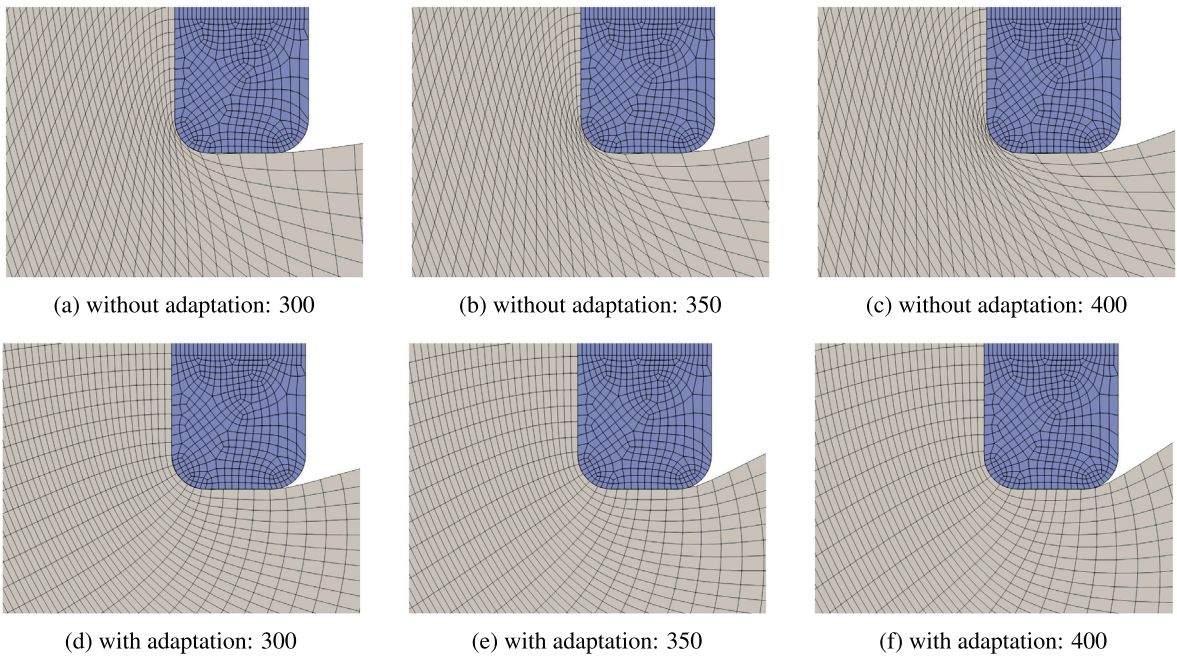
4. Numerical results

In this section we show the capabilities of the proposed mesh adaptation scheme using different numerical examples. In the following examples, the basic units kg, mm, s, and K are used.
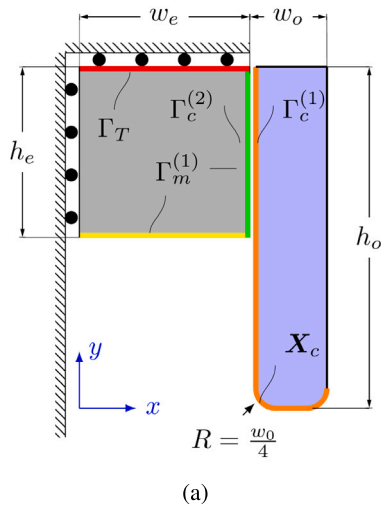
Quantity	Value
height h_e	1
width w_e	1
thickness t_e	0.1
height h_o	2
width w_o	1/4
thickness t_o	0.1

(a)   (b)

Fig. 11. Example 1: Problem setup with a grey body denoting the expanding material and a violet body representing the rigid obstruction. (a) geometry and boundary conditions (b) dimensions. A temperature surface Dirichlet boundary condition is applied at Γ_T (red line). Moreover, all other boundaries of expanding material are modeled adiabatic. The thermo-mechanical contact slave ($\Gamma_c^{(1)}$) and master ($\Gamma_c^{(2)}$) boundaries are represented using in orange and green lines. For the mesh adaptation the mesh sliding surfaces ($\Gamma_m^{(1)}$) are denoted by green and yellow lines. (For interpretation of the references to color in this figure legend, the reader is referred to the web version of this article.)

(a) without adaptation: 300   (b) without adaptation: 350   (c) without adaptation: 400

(d) with adaptation: 300   (e) with adaptation: 350   (f) with adaptation: 400

Fig. 12. Example 1: Mesh around the corner (a)–(c) without mesh adaptation and (d)–(f) with mesh adaptation for time steps 300, 350, and 400, respectively.

4.1. Expansion past a rigid obstruction

As the first numerical example, we explore a pseudo 2-dimensional expansion past a rigid body as illustrated in Fig. 11. The geometry and the boundary conditions are depicted in Fig. 11(b) and the corresponding dimensions are given in Fig. 11(a). The expanding material is modeled as presented in Section 2.2. It's elastic behavior described by Ψ_e is modeled using a Neo-Hookean material model with parameters listed in Table 1. The expansion is restricted to $+x$ and $-y$ direction by arresting the normal displacements as shown in Fig. 11(b). Furthermore, the initial temperature T_0 is set to 198 and a temperature surface Dirichlet boundary condition $T = 148 + 345 \log_{10}(1 + [(8 \times (t+3))/60])$ is applied to Γ_T. Moreover, all other boundaries are modeled adiabatic. Finally, to avoid 3-dimensional effects, the displacements in z−direction are arrested. Both, the expanding and the rigid body are
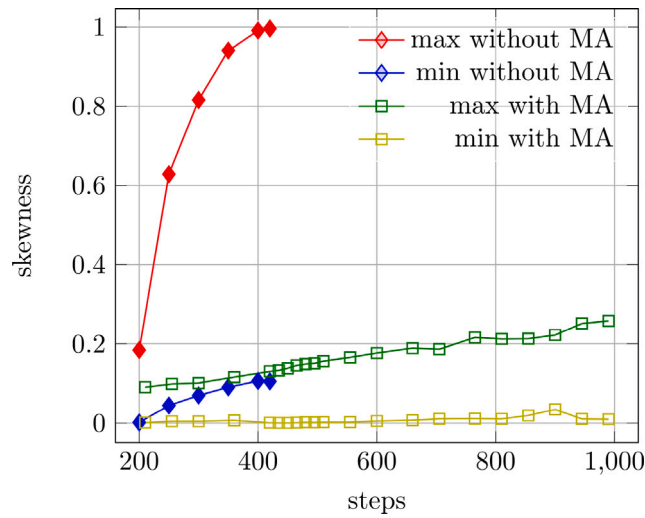
Fig. 13. Example 1: Comparison of minimum and maximum skewness over time steps in the corner region around X_c with radius $r = 0.1$ for the problem with and without mesh adaptation (MA).

discretized with 8-noded hexahedral elements with 22,500 elements (45,602 nodes) and 6414 elements (13,092 nodes) with one element in the thickness direction, respectively. For the mortar thermo-mechanical contact, the outer surface of the rigid body is chosen as the slave side and the surface of the expanding material as the master side. The contact interface is discretized with 4-noded quadrilateral elements, where the contact penalty parameter is set to $\epsilon_c = 1 \times 10^8$ and the interface conductivity to $\beta_c = 0$, i.e., modeling adiabatic contact. The thermo-mechanical problem is analyzed for 1000 steps using a time step size $\Delta t = 0.05$. The nonlinear system of equations resulting in each time step is solved using a Newton–Raphson scheme with a tolerance on the combined residual and increment of 10^{-8}. The linear monolithic thermomechanical system to be solved in each Newton iteration is approached by means of an iterative GMRES method with AMG(BGS) preconditioner. The convergence tolerance for the linear solver is set to 10^{-10}.

The accompanying mesh adaptation problem is formulated as follows: to achieve a good quality mesh around the corner X_c (see Fig. 11(b)), we employ a mesh localization as in (46) and (47) with $c = 100$. The target element edge length (l_{r0}^i) in each time step are estimated as in (45) and mesh refitting parameters as listed in Table 2. The mesh sliding surfaces $\Gamma_m^{(1)}$ in reference configuration are portrayed in the Fig. 11(b). For the Newton–Raphson scheme the convergence tolerance for the residual and the displacement increment is set to 10^{-5}. Moreover, the linearized system is solved with the "SuperLU" [45] direct solver. After the mesh refitting step, data needs to be transferred from the old to the new mesh. For the material model as presented in Section 2.2, the computation of the inelastic deformation gradient F_{in}^{n+1} requires F_{in}^n, F^n, S^n, and T^n. These quantities have to be transferred to the new mesh. The tensor data F_{in}^n is transferred by the "R-MLS" method with quadratic basis (see Section 3.2.2), the deformation gradient F^n is reconstructed from nodal displacements, and the stress S^n and temperature T^n are interpolated as scalar using moving least square with quadratic basis (see Section 3.2.1). The mesh adaptation is carried out every 15th step starting from step 210. Finally, the computation is carried out on 2 nodes (48 CPUs) of a computing cluster with Intel Xeon E5-2680v3 2.5 GHz processors.

First, the results without adaption are investigated. As expected, once the expanded material passes the corner, the mesh quality reduces (see Figs. 12(a)–12(c)). The element skewness around the corner X_c in the radius 0.1 is plotted over time in Fig. 13. The element skewness is computed as

$$skewness = \max\left(\frac{\theta_{max} - 90}{180 - 90}, \frac{90 - \theta_{min}}{90}\right) \quad \in [0, 1], \tag{54}$$

where θ_{max} and θ_{min} are the maximum and minimum included angle (in degree) between the edges. For a cuboid shape $\theta_{max} = \theta_{min} = 90°$ and the skewness is zero (optimal element quality). In contrast, when $\theta_{max,min} \to 0$, corresponding to a very skewed element, the skewness value is 1 (worst element quality). From Fig. 13 it can be seen that the skewness increases rapidly, starting from time step 200 to 425. After step 250, the maximum skewness is greater than 0.6, which may affect the accuracy of the solution. At time step 425 (see Fig. 14(a)), the elements are heavily distorted (skewness ≈ 1) such that computation can no longer be continued. However, a volume increase of about 863% is achieved at this step.

Next, the results including the proposed mesh adaptation scheme are studied. The mesh around the corner is portrayed in Figs. 12(d)–12(f) and 14(b). Compared to the results without mesh adaptation, a mesh of higher quality is maintained around the corner (X_c) during the expansion. The skewness near the corner is greatly reduced throughout the simulation (see Fig. 13). A slight increase in skewness can be attributed to the extreme volume expansion and shape change which cannot be completely avoided. Fig. 14(b) shows the expanded state at step 425, which has exhibits a significantly improved mesh quality as compared to the simulation without mesh adaptation (see Fig. 14(a)). Moreover, further states at steps 800 and 1000, that could only be
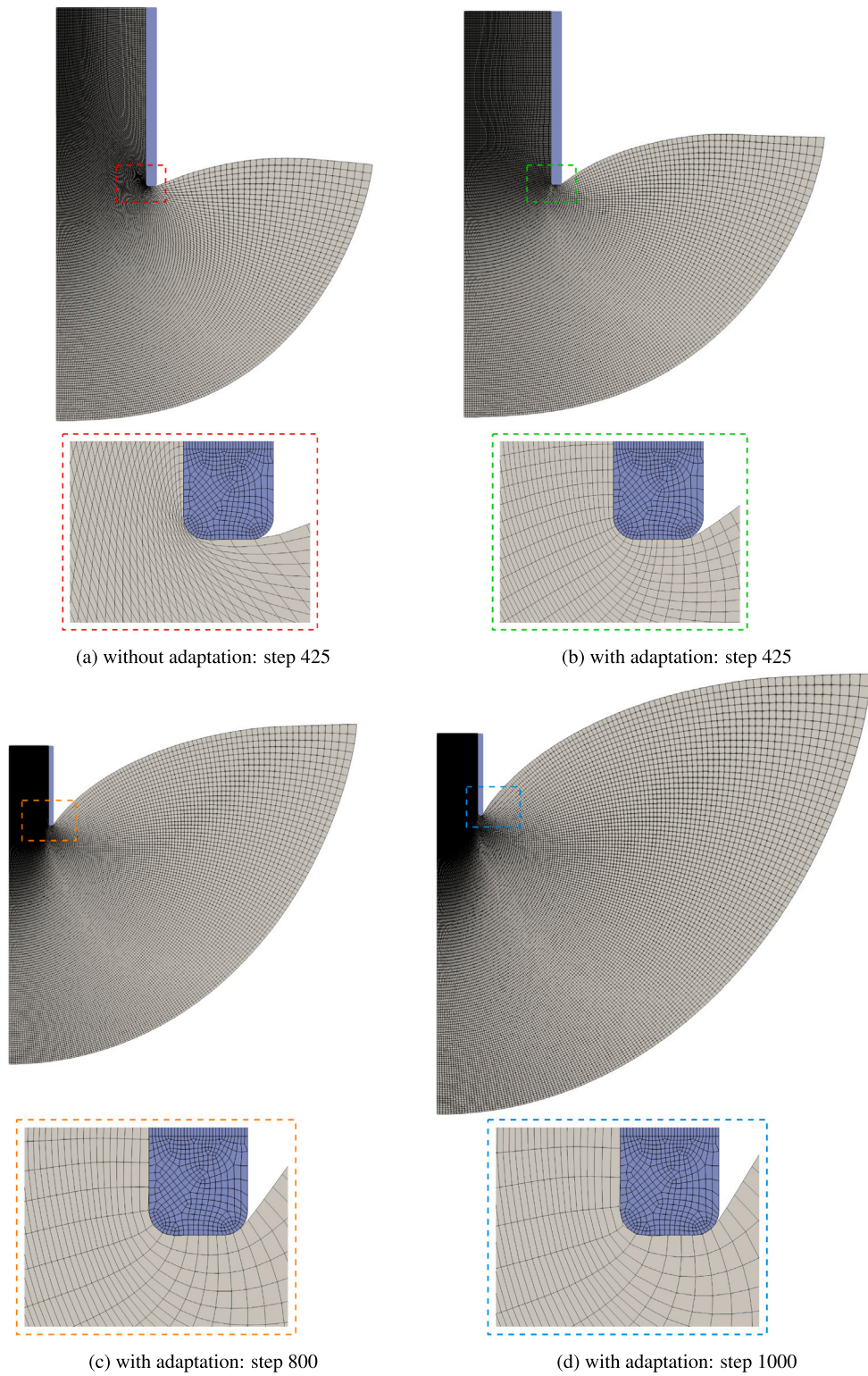
(a) without adaptation: step 425

(b) with adaptation: step 425

(c) with adaptation: step 800

(d) with adaptation: step 1000

Fig. 14. Example 1: Deformed state at step (a) 425 without adaptation, (b) 425 with adaptation, (c) 800 with adaptation, and (b) 1000 with adaptation.
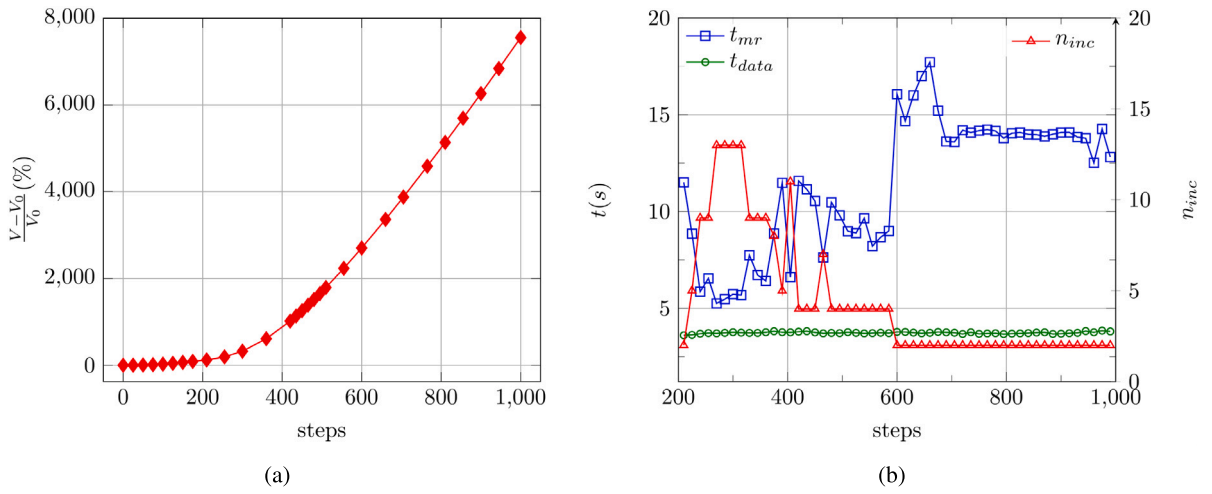
Fig. 15. Example 1: (a) percentage increase in total volume ($\frac{V-V_0}{V_0}$) vs. step. (b) computation time for mesh refitting step t_{mr} per incrementation steps n_{inc} and data mapping t_{data} time for each mesh adaptation step.

(a) without mesh adaptation at step 420

(b) with mesh adaptation at step 420
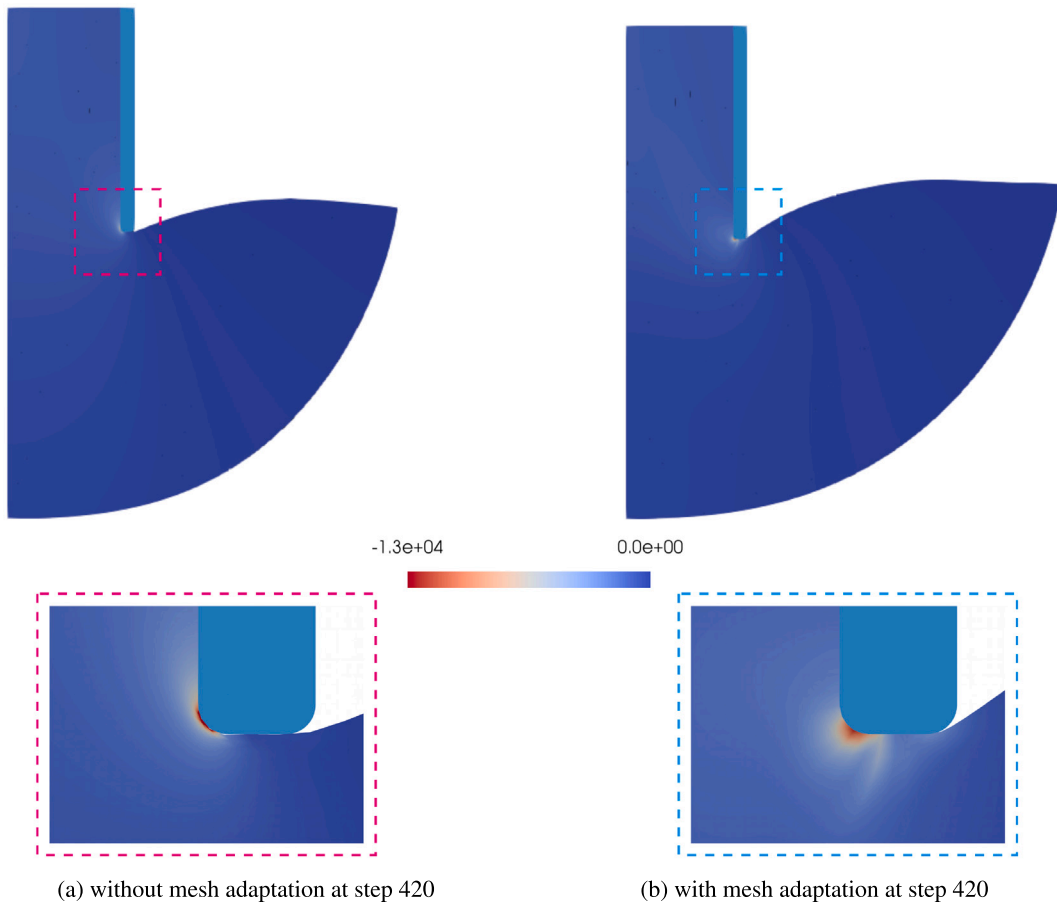
Fig. 16. Example 1: Comparison of first principal Cauchy stress (maximum compressive in MPa) at step 420. Subfigures (a) without mesh adaptation and (b) with mesh adaptation.
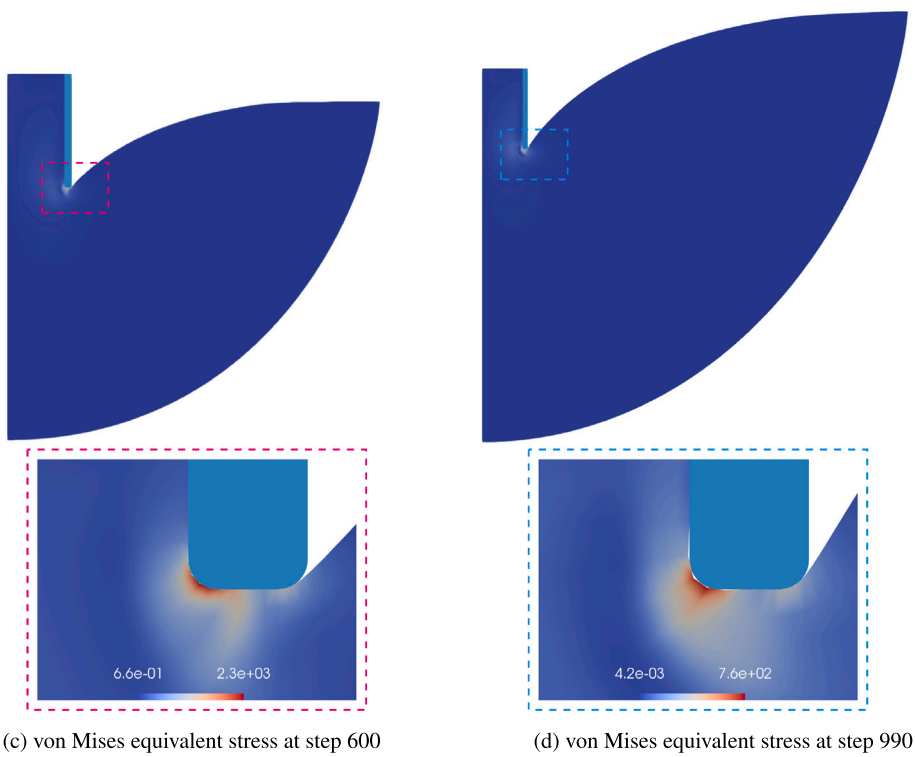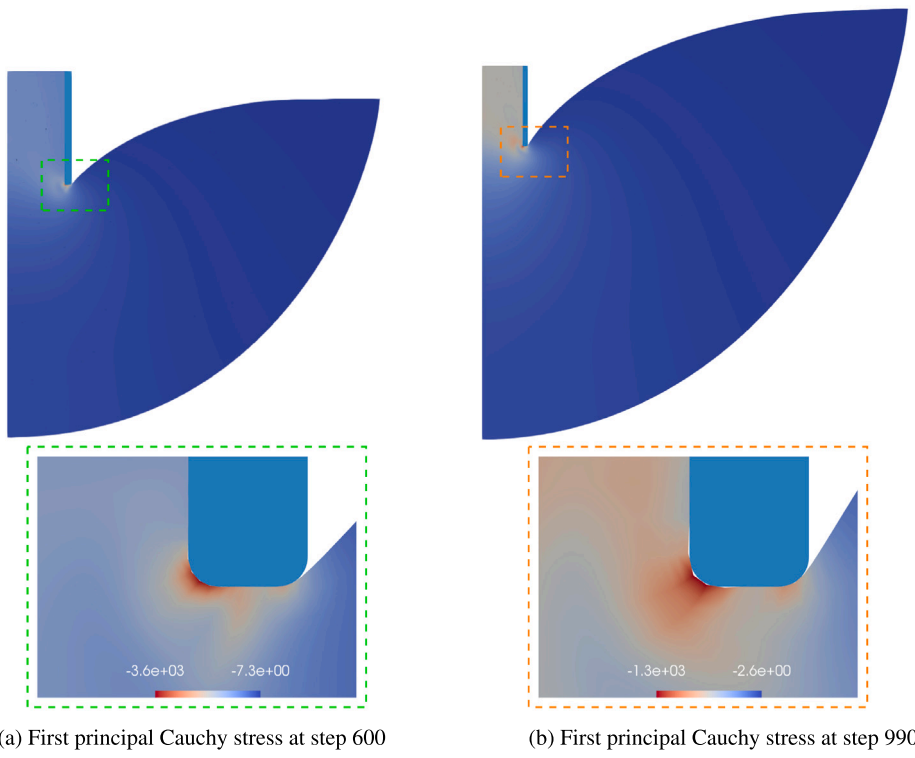
(a) First principal Cauchy stress at step 600

(b) First principal Cauchy stress at step 990

(c) von Mises equivalent stress at step 600

(d) von Mises equivalent stress at step 990

Fig. 17. Example 1: von Mises equivalent stress and first principal Cauchy stress (maximum compressive in MPa) at steps 600 and 990 with mesh adaptation.
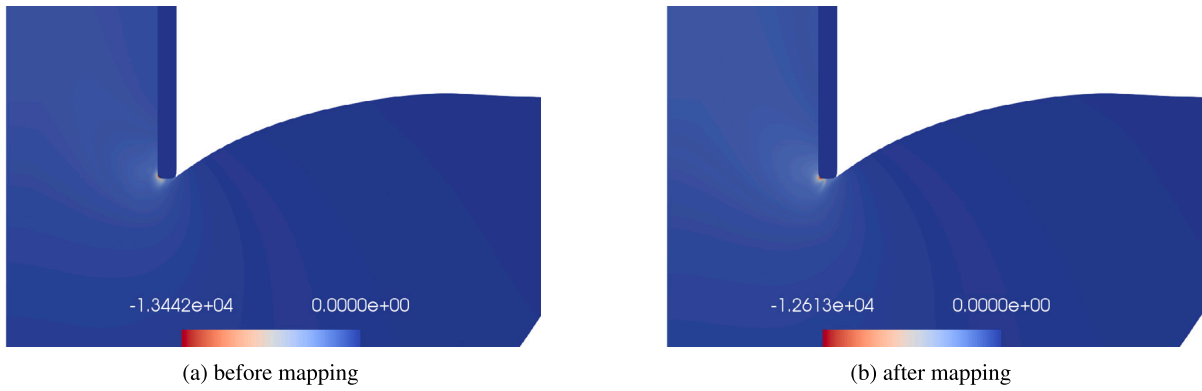
(a) before mapping

(b) after mapping

Fig. 18. Example 1: Comparison of first principal Cauchy stress (maximum compressive in MPa) at step 420 before and after data mapping.

Table 3
Material properties of the deformable body.

Parameter	Value
Young's modulus (E)	1×10^4
Poisson's ratio (v)	0.3
Thermal conductivity (k_0)	7.55×10^6
Heat capacity (c_v)	1.4×10^{-2}

produced/reached when the mesh adaptation is activated, are portrayed in Figs. 14(c) and 14(d). At the end of step 1000, there is a volume increase of approximately 7553%. The increase in volume over time steps is depicted in Fig. 15(a). The mesh quality at step 1000 with a volume expansion of 7553% is still significantly better as compared to the simulation without MA at step 425 (at which the volume increase is only 863%). It has been tested that the expansion process could even be carried out further, which confirms the robustness of the overall numerical solution scheme.

To get insights into the physical behavior of the investigated material, the first principal Cauchy stress is plotted. The Cauchy stress is obtained from interpolated second Piola–Kirchhof stress tensor (see Section 2.2). The first principal Cauchy stress at step 420 resulting from simulations with and without MA is plotted in Fig. 16. At step 420, mesh resulting from a simulation without MA is heavily distorted (c.f Fig. 14(a)), leading to a rather unphysical stress distribution, namely very high peak stresses within distorted finite elements in boundary layer, which abruptly drop to significantly smaller stress values in next finite element layers (see Fig. 16(a)). In contrast, simulation with MA leads to physically more reasonable, i.e., smoother, stress distributions, but still with highest stress values occurring in boundary region near sharp corner at X_c (see Fig. 16(b)). Furthermore, first principal Cauchy stress at steps 600 and 990, plotted in Figs. 17(a) and 17(b), shows a similar trend. As a result, von Mises equivalent stress exhibits its peak values in this boundary region, as depicted in Figs. 17(c) and 17(d). Finally, Fig. 18 shows the stress distribution before and after data mapping for step 420. There is a discretization error of approximately 6.1% in the peak value of the stresses, which can be attributed to the polynomial approximation of the stress field in the data mapping procedure. This aspect along with the consistent spatial convergence behavior of the data mapping scheme is addressed in the author's previous publication [22].

The computation time for the mesh adaptation is plotted in Fig. 15(b). The figure portrays the time for the mesh refitting t_{mr} per incrementation step n_{inc} and the data mapping time t_{data} for every mesh adaptation step. Furthermore, the total time for the mesh adaptation step can be computed as $t_{mr} n_{inc} + t_{data}$. Time t_{mr} is the total time spent for the MR including all the necessary setup. For $n_{inc} > 1$, also the time spent on the unconverged Newton–Raphson iterations is included. On average t_{mr} is 13 s. The data transfer time t_{data} is 4 s and approximately constant. In the initial phase, specifically between steps 200 to 400 (see Fig. 15(a)) the number of incrementation steps range between 5 to 13. However, as we progress, the incrementation requirement decreases significantly. From steps 600 to 1000, only two steps are needed for each mesh adaption. During the simulation a total of 52 MA steps were performed with an average computational time per mesh adaptation step of 56 s. The total simulation time is 10,960 s, i.e., the mesh adaptation accounts for a share of approximately 27%.

4.2. Expansion past a rigid obstruction and a deformable body

This example is an extension of the previous example, and the problem setup is illustrated in Fig. 19. The dimensions, material properties, boundary conditions, and discretization of the expanding and rigid body are the same as in the previous example (see Fig. 11, Table 1). The length of the deformable body (green) is twice the length of the rigid body, has the same thickness as the rigid body, and boundary conditions as illustrated in Fig. 19. The material of the deformable body is of Neo-Hookean type with parameters as given in Table 3. For the thermomechanical mortar contact between the expanding and deformable body, the boundary of the expanding body is chosen as the master surface $\Gamma_c^{(2)}$ and the boundary of the deformable body as the slave surface
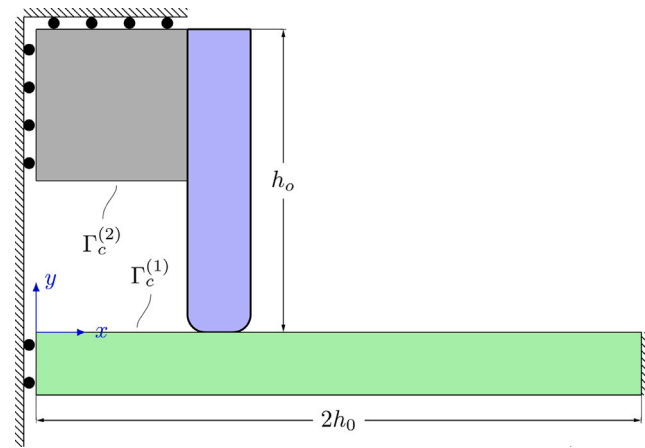
Fig. 19. Example 2: Problem setup with a grey body denoting the material in expansion. The blue and green bodies represent the rigid body, and the deformable body, respectively.

$\Gamma_c^{(1)}$ (see Fig. 19). Furthermore, the penalty parameter for this contact pair is set to 1×10^7, and the interface conductivity is $\beta_c = 0$, i.e., adiabatic contact. The deformable body is discretized with 420 linear hexahedral elements. The thermo-mechanical problem is analyzed for 500 time steps with a step size of $\Delta t = 0.05$. The nonlinear system of equations resulting in each time step is solved using a Newton–Raphson scheme with a tolerance on the combined residual and increment of 10^{-8}. Again, the linearized monolithic thermomechanical system is solved using the iterative GMRES method with AMG(BGS) preconditioner with a tolerance of 10^{-10}.
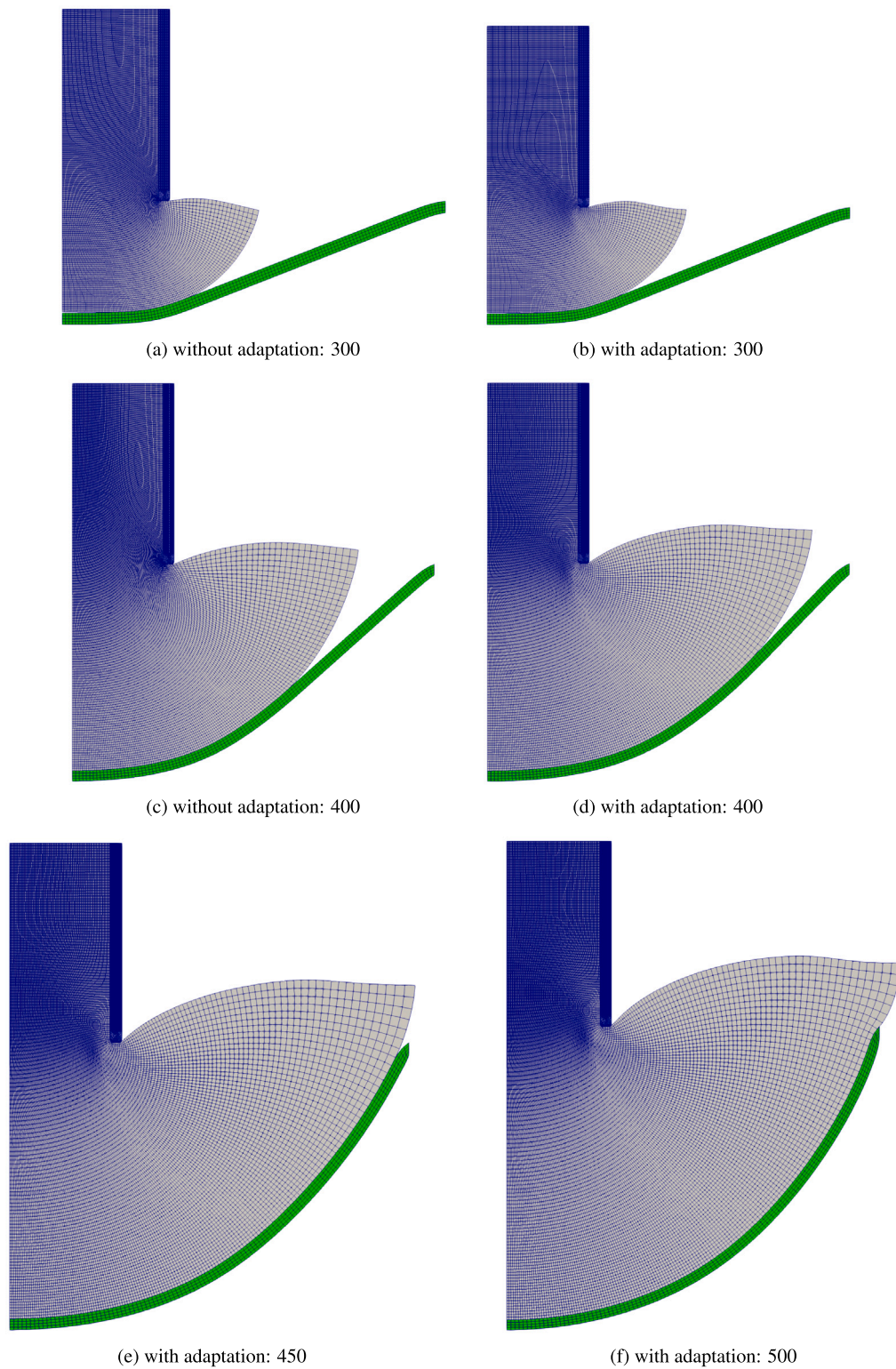
The mesh adaptation problem is formulated as follows: Like in the previous example, to achieve a high mesh quality around the corner X_c, we employed a mesh localization according to (46) and (47) with $c = 100$. The target element edge length (l_{r0}^i) in a time step are estimated as in (45). The mesh refitting parameters are the same as for the previous example and are listed in Table 2. The convergence tolerance for the residual and displacement increment is chosen to 10^{-5} and the linearized system is solved with the "SuperLU" solver. Again, the data transfer parameters remain the same as in the previous example. The mesh adaptation is carried out every 5th step starting from step 200. Finally, the computation is carried out on 3 nodes (72 CPUs) of a computing cluster with Intel Xeon E5-2680v3 2.5 GHz processors.

The mesh resulting from a simulation of the expansion process without and with mesh adaptation is depicted for the time steps 300 and 400 in Figs. 20(a)–20(d), respectively. The mesh near the corner point X_c (not plotted) shows the same trend as in the previous example (see Fig. 12). The simulation without mesh adaptation in this example fails at step 400 due to a heavily distorted mesh near X_c, leading to non-convergence of the Newton–Raphson scheme. The deformed states resulting from the simulation with mesh adaptation at time steps 450 and 500 are depicted in Figs. 20(e) and 20(f), respectively. Also in this example, the proposed MA approach results in a significantly improved mesh quality compared to simulations without MA. The additional presence of the deformable body in this second example is motivated by a practical application scenario within our broader research interests, considering seals for such expandable foams. It is demonstrated that even for this highly challenging scenario, i.e., extreme volume expansion of a foam squeezed through the gap between a rigid and a deformable body including mutual thermo-mechanical contact interaction, the proposed MA approach allows for a high mesh quality and robust simulations.

Finally, the computational costs for the mesh adaptation procedure are presented in Fig. 21. In contrast to the previous example, less incrementation steps (≤ 2) are necessary as the mesh adaption frequency is higher. The data transfer time is ≤ 3 s and t_{mr} is 15 s on average. Finally, a total of 60 MA steps are performed during the simulation with an average computation time of 20 s spent for MA. The total simulation time is 5621 s for this example, i.e., the mesh adaptation accounts for a share of $\approx 20\%$.

4.3. Inward expansion of a hollow cylinder past a rigid obstruction

Next, the proposed MA approach shall be applied to a complex 3D problem. Thereto, the inward expansion of a hollow cylinder past a rigid obstruction is investigated. Consider the problem setup depicted in Fig. 22. Due to symmetry, only a quarter portion of the system is simulated. The hollow quarter cylinder has an outer radius of $r_{eo} = 4$, an inner radius of $r_{ei} = 3$, and a length of $l_e = 1$. The rigid body has the same outer radius as the hollow cylinder's, an inner radius of $r_{oi} = 2.5$, and a length of $l_o = 0.5$. The corner radius of the rigid obstruction has the same dimensions as in Example 1 (see Fig. 11). Also the material model for the expanding body is the same as in Example 1 (Section 4.1). The initial temperature T_0 is set to 198 and a temperature surface Dirichlet boundary condition according to $T = 148 + 345 \log_{10}(1 + [(8 \times (t + 3))/60])$ is applied at the outer surface of the expanding cylinder denoted by Γ_T. Moreover, all other boundaries of expanding material are modeled adiabatic. Apart from the symmetry boundary conditions (see Fig. 22), for the structural problem also the outer surface of the expanding cylinder (denoted by Γ_u) is fixed. Both, the expanding and the rigid body are discretized with 8-noded hexahedral elements with $432,000$ elements (449631 nodes) and 14700 elements (18178 nodes), respectively. For the mortar thermo-mechanical contact, the outer surface of the rigid body is chosen as

(a) without adaptation: 300

(b) with adaptation: 300

(c) without adaptation: 400

(d) with adaptation: 400

(e) with adaptation: 450

(f) with adaptation: 500

Fig. 20. Example 2: (a) and (c) show the mesh without mesh adaptation at steps 300 and 400, respectively; (b) and (d) show the corresponding meshes with mesh adaptation. (e) and (f) mesh at steps 450 and 500 with mesh adaptation, respectively.
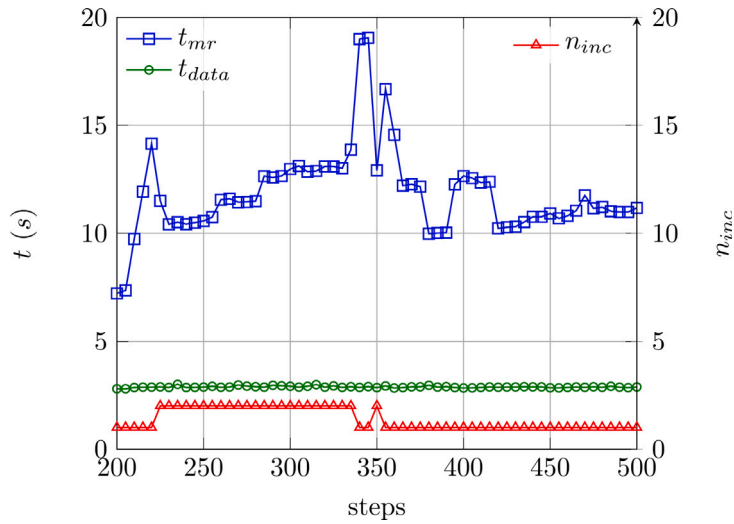
Fig. 21. Example 2: Computation time for mesh refitting step t_{mr} per incrementation steps n_{inc} and data mapping t_{data} time for each mesh adaptation step.
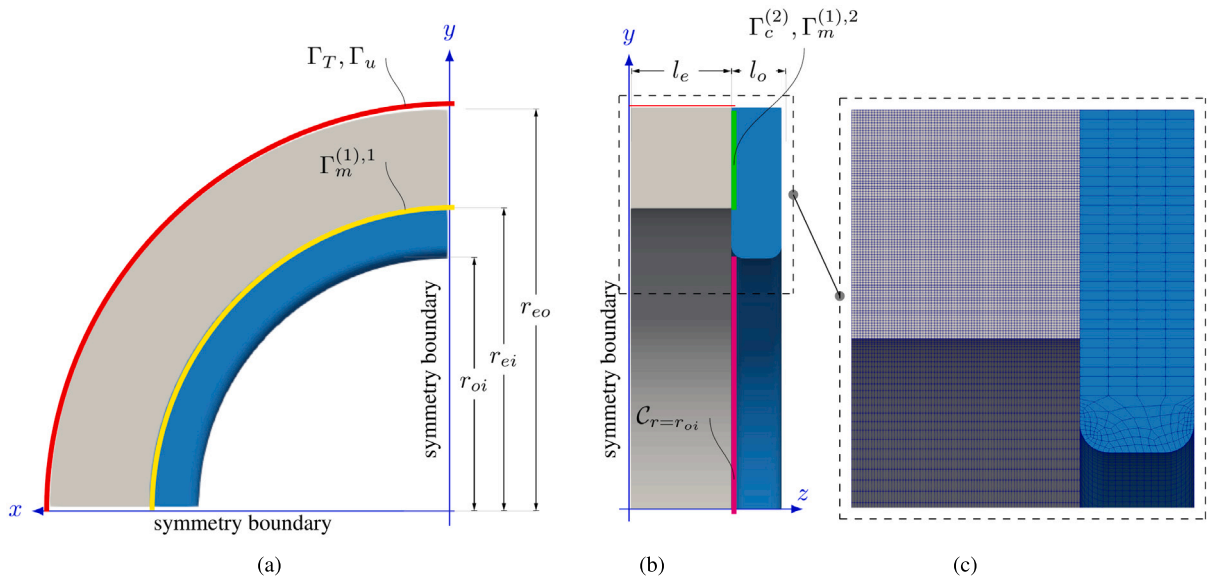

(a)   (b)   (c)

Fig. 22. Example 3: expanding material (gray), obstruction (blue), and auxiliary boundary (green) (a) +z-plane view (b) +x-plane view (same as +y-plane due to symmetry). (c) mesh at reference configuration. The temperature and displacement surface Dirichlet boundaries (Γ_T, Γ_u) are represented by a red line. Furthermore, all other boundaries of expanding material are modeled adiabatic. The master side ($\Gamma_c^{(2)}$) of the thermo-mechanical contact is denoted by green line. The mesh sliding surfaces ($\Gamma_m^{(1)}$) for the mesh adaptation are represented by green and yellow lines. Finally, magenta line represent a curve $C_{r=r_{oi}}$.

the slave side and the surface of the expanding material as the master side ($\Gamma_c^{(2)}$). The contact interface is discretized with 4-noded quadrilateral elements. Moreover, the penalty parameter is set to $\epsilon_c = 10^8$ and the interface conductivity to $\beta_c = 0$, i.e., adiabatic. The thermo-mechanical problem is analyzed for 500 steps with time step size $\Delta t = 0.05$ using Newton–Raphson scheme with a convergence tolerance of 10^{-8} on the combined residual and increment. Again, the linearized monolithic thermomechanical system is solved using the iterative GMRES method with AMG(BGS) preconditioner with tolerance 10^{-10}.

The mesh adaptation problem is formulated as follows: To achieve a high mesh quality around the corner edge $C_{r=r_{oi}}$ (see Fig. 22), we employ a mesh localization according to (46) with l_{r0}^i as in (45). The function $f(X)$ as shown in (47) is reformulated according to

$$f(X) = 1 + \exp\left(-c \left(r_n^2 + r_{ei}^2 - 2r_n r_{ei} + (z - l_e)^2\right)\right),\tag{55}$$

with $r_n = x^2 + y^2$ and $c = 150$. The mesh refitting parameters are the same as in the previous example (see Table 2). The mesh sliding surfaces are denoted by $\Gamma_m^{(1),1}$ and $\Gamma_m^{(1),2}$ in Fig. 22. The convergence tolerance of the Newton–Raphson scheme is set to 10^{-5}.
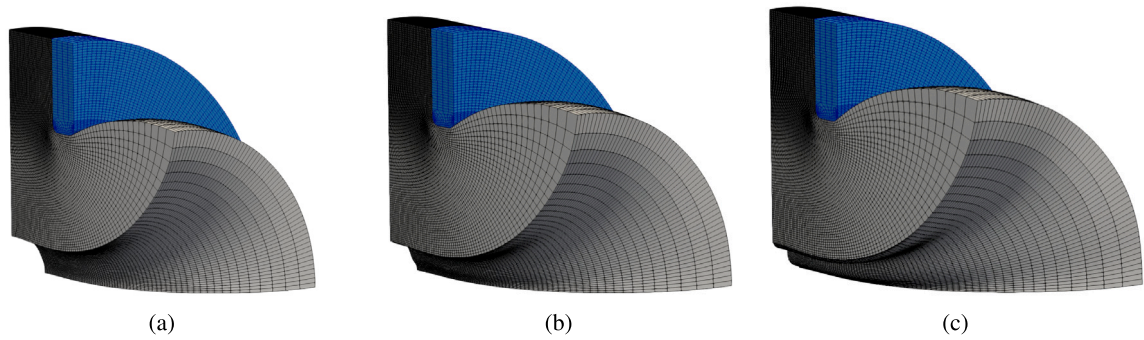
<center>(a)   (b)   (c)</center>

Fig. 23A. Example 3: deformed state at step (a) 360 (b) 400 (c) 428.

In contrast to previous examples, the linearized system is solved iteratively using the GMRES method with an AMG preconditioner. Furthermore, the convergence tolerance of the linear solver is set to 10^{-10}. The data transfer for scalars is done using a moving least squares scheme with trilinear shape functions and for tensors using the 'R-MLS' variant with trilinear basis as described in Section 3.2.2. The mesh adaptation is carried out every 5th step starting from step 100. The computation is carried out on 9 nodes (216 CPUs) of a computing cluster with Intel Xeon E5-2680v3 2.5 GHz processors.

The deformed states at time steps 360, 400, and 428 are depicted in Figs. 23A and 23B. In step 428, mechanical instabilities, i.e. local buckling phenomena, are observed in the system, an effect that is particularly challenging with respect to mesh quality. At this step, the expanded material almost closes the annular opening leading to a minimum inner radius of approximately 0.3545 (= 0.118 r_{ei}). The von Mises equivalent stress at steps 360, 400, and 425 is depicted in Fig. 24. Like in the previous example, the equivalent stress is initially higher in the region near the fillet $C_{r=r_{oi}}$ (see Figs. 24(a), 24(d), 24(g) and 24(j)). But once mechanical instabilities start to form, the position of the peak value of the equivalent stress shifts towards the kinks resulting from the buckling as portrayed in Figs. 24(b), 24(c), 24(e), 24(f), 24(h), 24(i), 24(k) and 24(l).

The volume increase during expansion is showcased in Fig. 25(a) with a final volume increase of 525%. Again, similar to the previous examples, the quality of the mesh in the vicinity of the rigid body (Figs. 23B(g)–(i)) is preserved. The minimum and maximum skewness (see (54)) change in the region around the curved edge $C_{r=r_{oi}}$ over time is depicted in Fig. 25(b). To isolate this most critical region around the curved edge for the post-processing, only contributions from elements satisfying the condition $0.8 < f(\boldsymbol{X}_e) < 1.0$ were considered in Fig. 25(b), where $f(\boldsymbol{X}_e)$ is given by (55) with $c = 1$ and $\boldsymbol{X}_e$ is the element centroid position. It can be seen that the skewness is < 0.15 in this critical region during the entire expansion process, which indicates a very high mesh quality.

Finally, the computational costs are shown in Fig. 26. The mesh adaptation problem is solved in a single step, i.e., $n_{inc} = 1$. The timing for one data transfer step is approximately 50 s on average, and the average timing for a mesh refitting step is around $t_{mr} = 70$ s. Finally, the total simulation time is approximately 27 h for this example, wherein the total computational time required for mesh adaptation accounts for a share of only $\approx 5\%$. This underlines again the efficiency of the proposed mesh adaptation approach, in particular when comparing it to remeshing schemes.

5. Conclusion

In the present work, a novel mesh adaptation scheme has been proposed for finite element-based models of mechanical, or more general multi-physics, problems involving a strong mesh distortion. The central building block of this mesh adaptation scheme is a novel mesh refitting approach, also denoted as mesh regularization, based on the definition of an element distortion potential considering contributions from different distortion modes such as skewness and aspect ratio of the elements. The regularized mesh is obtained by minimizing this potential. Moreover, based on the concept of spatial localization functions, the method allows to specify tailored requirements on mesh resolution and quality for regions with strongly localized mechanical deformation and mesh distortion. To address also problems involving significant surface deformation, the usage of a mortar mesh-sliding scheme has been proposed to allow for a tangential motion of boundary nodes without changing the boundary topology. To transfer tensor-valued history data from the old to the new mesh, the novel mesh refitting approach is combined with structure-preserving tensor interpolation schemes as proposed in our previous work [22].

Based on two elementary test cases, i.e. large deformation mechanical problems involving frictional contact interaction, it has been demonstrated that the mesh refitting approach together with the mesh-sliding scheme enables a significantly improved mesh relaxation as compared to approaches with fixed boundary nodes. Moreover, as a practically relevant application scenario, the thermo-mechanical expansion of materials such as foams involving extreme volume changes by up to two orders of magnitude along with large and strongly localized strains as well as thermo-mechanical contact interaction has been considered. For this scenario it has been demonstrated that the proposed regularization approach preserves a high mesh quality with a maximal element skewness below 30%. Moreover, in the investigated numerical examples, the computation time for mesh adaptation was typically in the order of only a few percent of the total simulation time. In contrast, simulations without mesh adaption have been shown to lead to

<center>28</center>

(d)
(e)
(f)

(g)
(h)
(i)

(j)
(k)
(l)

(m)
(n)
(o)
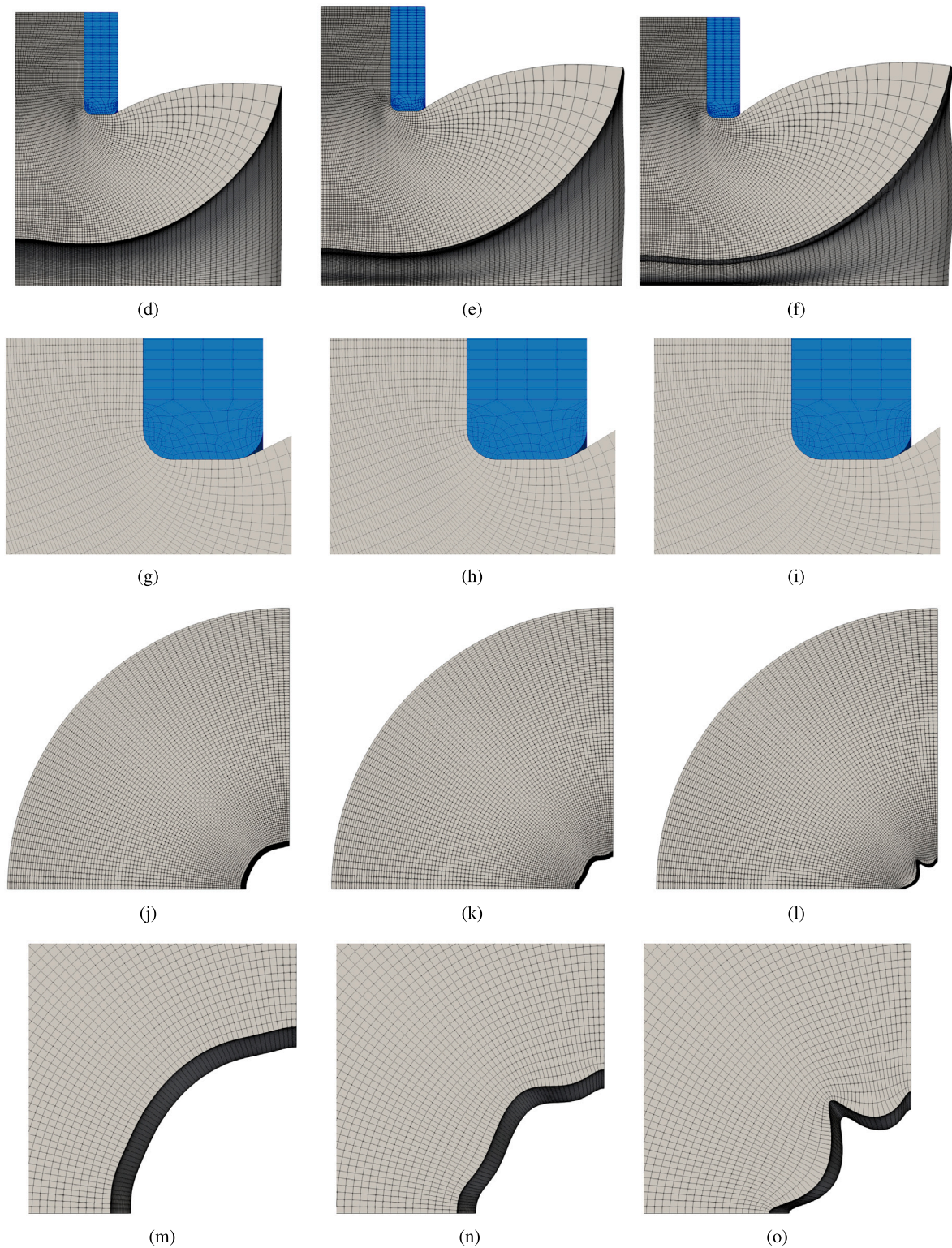
Fig. 23B. Example 3: Deformed states at steps 360, 400, and 428 are illustrated in columns 1, 2, and 3, respectively. Row 1: +x-plane view, Row 2: +x-plane detailed view around the fillet, Row 3: +z-plane view, and Row 4: +z-plane detailed view at the center (c.f. Figs. 22(a) and 22(b)).
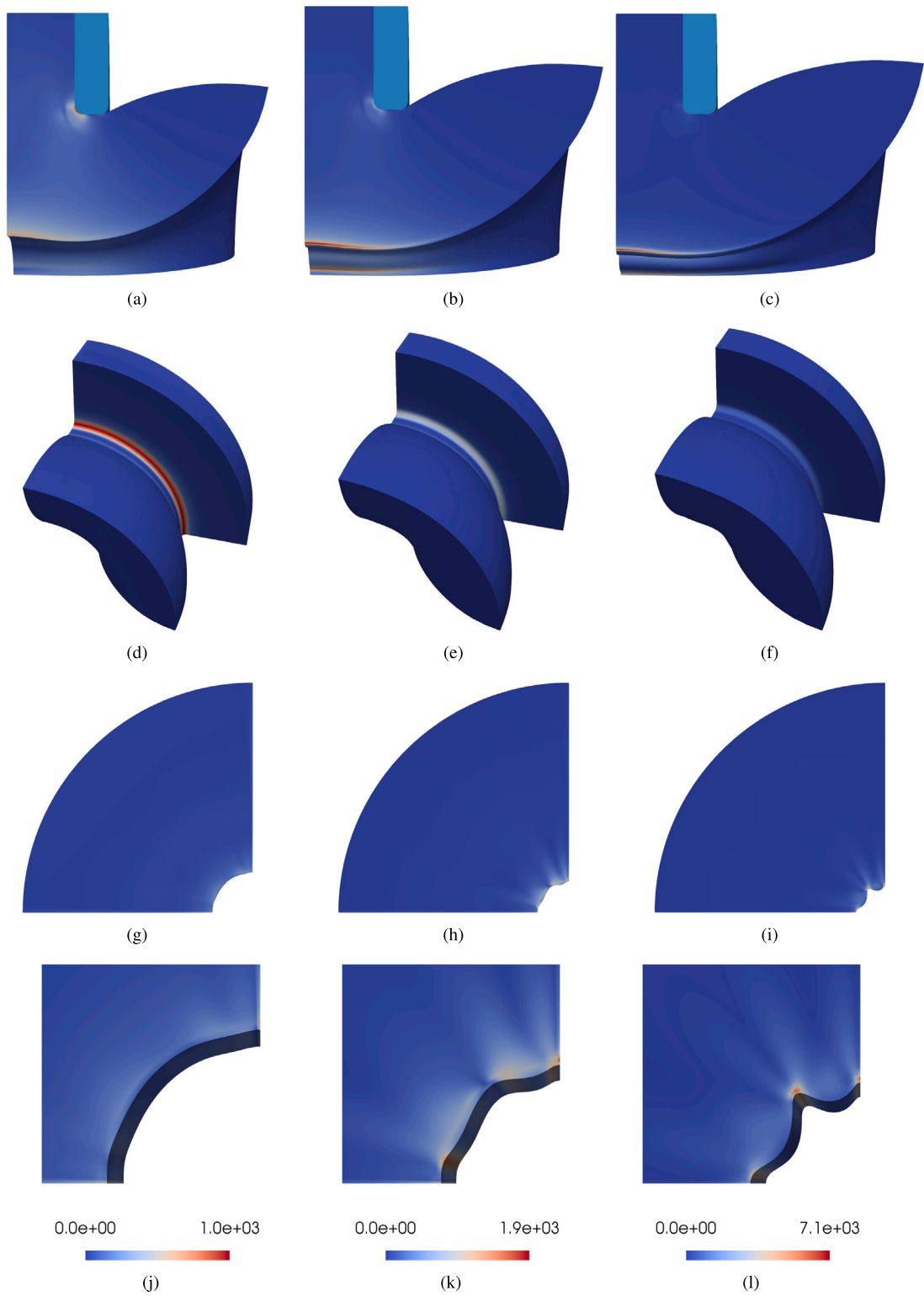
Fig. 24. Example 3: von Mises equivalent stress in MPa at steps 360, 400, and 425 are illustrated in columns 1, 2, and 3, respectively. Row 1: +x-plane view, Row 2: 3D view, Row 3: +z-plane view, and, Row 4: +z-plane detailed view at the center (c.f. Figs. 22(a) and 22(b)).
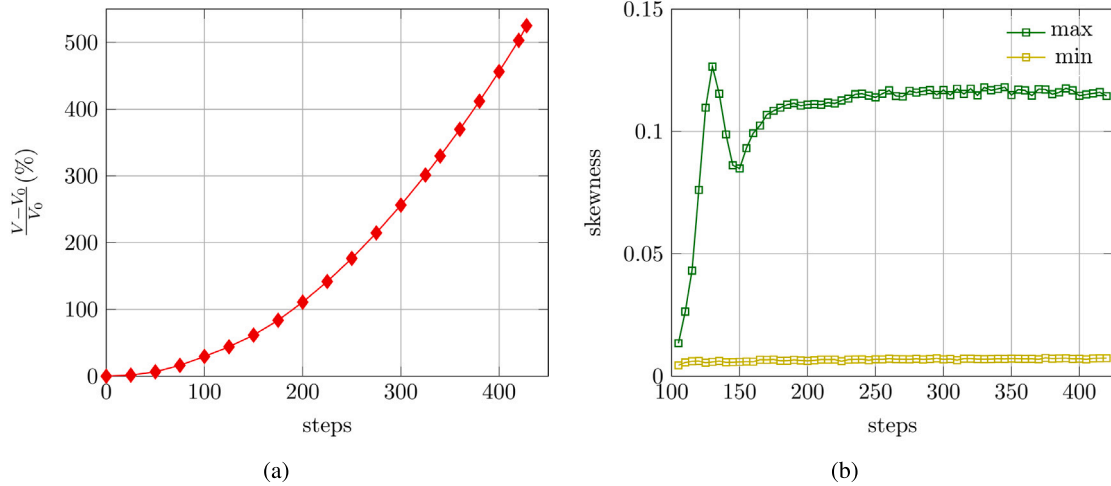
Fig. 25. Example 3: (a) percentage change in volume over time. (b) minimum and maximum skewness near the corner.
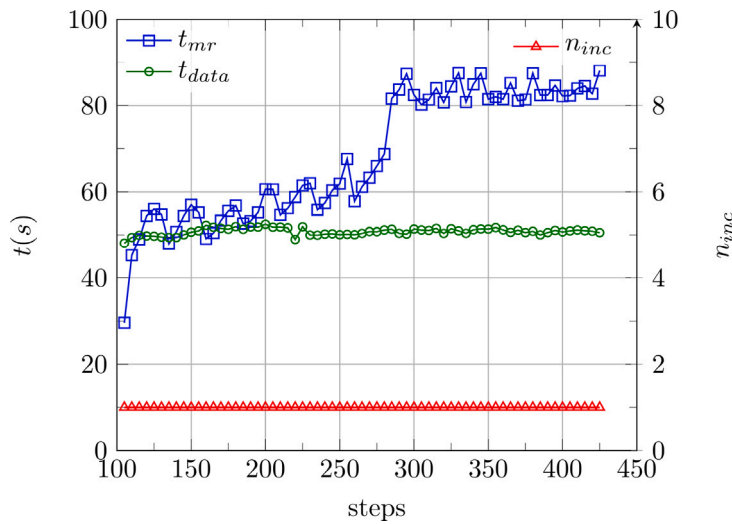

Fig. 26. Example 3: Computation time for mesh refitting step t_{mr} per incrementation steps n_{inc} and data mapping t_{data} time for each mesh adaptation step.

significant mesh distortion with larger element aspects ratios and a maximal element skewness close to 100%, i.e., neighboring element edges that are almost parallel, and eventually, to non-convergence of the numerical solution scheme.

In cases were the global shape change of the discretized mechanical body is very anisotropic, an increase of the element aspect ratios can be reduced, but not completely avoided, with regularization schemes that preserve the mesh connectivity. For such scenarios, a future combination of the proposed mesh regularization scheme with element subdivision procedures is considered promising.

CRediT authorship contribution statement

Abhiroop Satheesh: Writing – review & editing, Writing – original draft, Visualization, Validation, Software, Methodology, Investigation, Formal analysis, Data curation, Conceptualization. **Christoph P. Schmidt:** Writing – review & editing, Writing – original draft, Methodology, Conceptualization. **Wolfgang A. Wall:** Writing – review & editing, Supervision, Resources, Project administration, Funding acquisition, Conceptualization. **Christoph Meier:** Writing – review & editing, Writing – original draft, Supervision, Project administration, Methodology, Conceptualization.

Declaration of competing interest

The authors declare the following financial interests/personal relationships which may be considered as potential competing interests:

Data availability

No data was used for the research described in the article.

Acknowledgments

Appendix A. Residual and system matrix: distortion potential

For sake of simplicity, the distortion potential in (40) is denoted in a abstract from as

$$\pi_m = \sum_{k=1}^{nco} \frac{1}{2}\ \varepsilon_k\ G_k^2(\mathbf{d}), \tag{A.1}$$

where ε_k can be $\{\bar{\varepsilon}_E, \hat{\varepsilon}_E, \varepsilon_A\}$, $G_k \in \{\bar{G}_E^i, (\hat{G}_E)_j, G_A^{mn}\}$, and *nco* is the number of total constraints. The residual of the distortion potential is given as

$$\mathbf{f}_u^d = \frac{\partial \pi_m}{\partial \mathbf{d}} = \sum_{k=1}^{nco} \varepsilon_k\ G_k \frac{\partial G_k}{\partial \mathbf{d}}. \tag{A.2}$$

Exemplary the first derivative of $\bar{G}_E^i$ (37), $(\hat{G}_E)_j$ (38), and G_A^{12} (39) reads

$$\frac{\partial \bar{G}_E^i}{\partial \mathbf{d}} = \frac{\bar{\boldsymbol{v}}^i}{(\bar{\boldsymbol{v}}^i \cdot \bar{\boldsymbol{v}}^i)^{1/2}} \frac{\partial \bar{\boldsymbol{v}}^i}{\partial \mathbf{d}}, \tag{A.3}$$

$$\frac{\partial (\hat{G}_E)_j}{\partial \mathbf{d}} = \frac{1}{(\bar{\boldsymbol{v}}^i \cdot \bar{\boldsymbol{v}}^i)} \frac{\partial (\boldsymbol{v}_j^i \cdot \boldsymbol{v}_j^i)}{\partial \mathbf{d}} - \frac{((\hat{G}_E)_j + 1)}{(\bar{\boldsymbol{v}}^i \cdot \bar{\boldsymbol{v}}^i)} \frac{\partial (\bar{\boldsymbol{v}}^i \cdot \bar{\boldsymbol{v}}^i)}{\partial \mathbf{d}}, \tag{A.4}$$

$$\frac{\partial G_A^{12}}{\partial \mathbf{d}} = \frac{1}{\| \boldsymbol{v}_1^1 \| \| \boldsymbol{v}_1^2 \|} \frac{\partial (\boldsymbol{v}_1^1 \cdot \boldsymbol{v}_1^2)}{\partial \mathbf{d}} - \frac{1}{2} \frac{(\boldsymbol{v}_1^1 \cdot \boldsymbol{v}_1^2)}{(\boldsymbol{v}_1^1 \cdot \boldsymbol{v}_1^1)^{3/2} \| \boldsymbol{v}_1^2 \|} \frac{\partial (\boldsymbol{v}_1^1 \cdot \boldsymbol{v}_1^1)}{\partial \mathbf{d}} - \frac{1}{2} \frac{(\boldsymbol{v}_1^1 \cdot \boldsymbol{v}_1^2)}{(\boldsymbol{v}_1^2 \cdot \boldsymbol{v}_1^2)^{3/2} \| \boldsymbol{v}_1^1 \|} \frac{\partial (\boldsymbol{v}_1^2 \cdot \boldsymbol{v}_1^2)}{\partial \mathbf{d}}, \tag{A.5}$$

respectively. Next, linearization yields the system matrix $\mathbf{K}^d$ as

$$\mathbf{K}^d = \frac{\partial \mathbf{f}_u^d}{\partial \mathbf{d}} = \sum_{k=1}^{nco} \varepsilon_k\ \frac{\partial G_k}{\partial \mathbf{d}} \frac{\partial G_k}{\partial \mathbf{d}} + \sum_{k=1}^{nco} \varepsilon_k\ G_k \frac{\partial^2 G_k}{\partial \mathbf{d}^2}. \tag{A.6}$$

Finally, discrete matrix vector system:

$$\mathbf{K}^d \Delta \mathbf{d} = -\mathbf{f}_u^d. \tag{A.7}$$

Appendix B. Supplementary data

Supplementary material related to this article can be found online at https://doi.org/10.1016/j.cma.2024.117444.

References

[1] M.M. Selim, R.P. Koomullil, Mesh Deformation Approaches–A Survey, J.Phys. Math. 7 (2) (2016) 1–9.
[2] Joe F. Thompson, Zahir U.A. Warsi, C. Wayne Mastin, Numerical Grid Generation: Foundations and Applications, Elsevier North-Holland, Inc., 1985.
[3] Yong Zhao, Ahmed Forhad, A general method for simulation of fluid flows with moving and compliant boundaries on unstructured grids, Comput. Methods Appl. Mech. Engrg. 192 (39–40) (2003) 4439–4466.
[4] Aukje De Boer, Martijn S. Van der Schoot, Hester Bijl, Mesh deformation based on radial basis function interpolation, Comput. Struct. 85 (11–14) (2007) 784–795.
[5] John T. Batina, Unsteady Euler Airfoil Solutions Using Unstructured Dynamic Meshes, AIAA J. 28 (8) (1990) 1381–1388.
[6] Charbel Farhat, Christoph Degand, Bruno Koobus, Michel Lesoinne, Torsional springs for two-dimensional dynamic unstructured fluid meshes, Comput. Methods Appl. Mech. Engrg. 163 (1–4) (1998) 231–245.
[7] Frederic J. Blom, Considerations on the spring analogy, Internat. J. Numer. Methods Fluids 32 (6) (2000) 647–668.
[8] Carlo L. Bottasso, Davide Detomi, Roberto Serra, The ball-vertex method: a new simple spring analogy method for unstructured dynamic meshes, Comput. Methods Appl. Mech. Engrg. 194 (39–41) (2005) 4244–4264.
[9] P.I. Crumpton, M.B. Giles, Implicit time–accurate solutions on unstructured dynamic grids, Internat. J. Numer. Methods Fluids 25 (11) (1997) 1285–1300.
[10] Clarence Burg, Analytic study of 2D and 3D grid motion using modified Laplacian, Internat. J. Numer. Methods Fluids 52 (2) (2006) 163–197.

[11] Andrew A. Johnson, Tayfun E. Tezduyar, Mesh update strategies in parallel finite element computations of flow problems with moving boundaries and interfaces, Comput. Methods Appl. Mech. Engrg. 119 (1–2) (1994) 73–94.

[12] Wolfgang A. Wall, Fluid-Struktur-Interaktion mit stabilisierten Finiten Elementen (Ph.D. thesis), Universität Stuttgart, 1999.

[13] Lori A. Freitag, Patrick Knupp, Tetrahedral Element Shape Optimization via the Jacobian Determinant and Condition Number, Sandia National Lab.(SNL-NM), Albuquerque, NM (United States), 1999.

[14] Patrick Knupp, Matrix Norms & the Condition Number: A general framework to improve mesh quality via node-movement, Technical report,, Sandia National Lab.(SNL-NM), Albuquerque, NM (United States), 1999.

[15] Zhi Yang, Dimitri J. Mavriplis, Mesh Deformation Strategy Optimized by the Adjoint Method on Unstructured Meshes, AIAA J. 45 (12) (2007) 2885–2896.

[16] Olgierd C. Zienkiewicz, Jian Z. Zhu, A simple error estimator and adaptive procedure for practical engineering analysis, Internat. J. Numer. Methods Engrg. 24 (2) (1987) 337–357.

[17] Olgierd Cecil Zienkiewicz, Jian Zhong Zhu, The superconvergent patch recovery and a posteriori error estimates. Part 1: The recovery technique, Internat. J. Numer. Methods Engrg. 33 (7) (1992) 1331–1364.

[18] Olgierd Cecil Zienkiewicz, Jian Zhong Zhu, The superconvergent patch recovery and a posteriori error estimates. Part 2: Error estimates and adaptivity, Internat. J. Numer. Methods Engrg. 33 (7) (1992) 1365–1382.

[19] H. Gu, Z. Zong, K.C. Hung, A modified superconvergent patch recovery method and its application to large deformation problems, Finite Elem. Anal. Des. 40 (5–6) (2004) 665–687.

[20] Delphine Brancherie, Pierre Villon, Adnan Ibrahimbegovic, On a consistent field transfer in non linear inelastic analysis and ultimate load computation, Comput. Mech. 42 (2) (2008) 213–226.

[21] Temesgen M. Kindo, Tod A. Laursen, John E. Dolbow, Toward robust and accurate contact solvers for large deformation applications: a remapping/adaptivity framework for mortar-based methods, Comput. Mech. 54 (1) (2014) 53–70.

[22] Abhiroop Satheesh, Christoph P. Schmidt, Wolfgang A. Wall, Christoph Meier, Structure-Preserving Invariant Interpolation Schemes for Invertible Second-order Tensors, Internat. J. Numer. Methods Engrg. 125 (2) (2024) e7373.

[23] E.H. Lee, D.T. Liu, Finite-Strain Elastic-Plastic Theory with Application to Plane-Wave Analysis, J. Appl. Phys. 38 (1) (1967) 19–27.

[24] Edward K. Rodriguez, Anne Hoger, Andrew D. McCulloch, Stress-dependent finite growth in soft elastic tissues, J. Biomech. 27 (4) (1994) 455–467.

[25] V.A. Lubarda, A. Hoger, On the mechanics of solids with a growing mass, Int. J. Solids Struct. 39 (18) (2002) 4627–4664.

[26] Gerhard A. Holzapfel, Nonlinear Solid Mechanics: A Continuum Approach for Engineering Science, Meccanica 37 (4) (2002) 489–490.

[27] M. Dittmann, M. Franke, İ Temizer, C. Hesch, Isogeometric Analysis and thermomechanical Mortar contact problems, Comput. Methods Appl. Mech. Engrg. 274 (2014) 192–212.

[28] Daniel Pantuso, Klaus-Jürgen Bathe, Pavel A. Bouzinov, A finite element procedure for the analysis of thermo-mechanical solids in contact, Comput. Struct. 75 (6) (2000) 551–573.

[29] Markus Gitterle, A dual mortar formulation for finite deformation frictional contact problems including wear and thermal coupling (Ph.D. thesis), Technische Universität München, München, 2012.

[30] Alexander Seitz, Wolfgang A. Wall, Alexander Popp, A computational approach for thermo-elasto-plastic frictional contact based on a monolithic formulation using non-smooth nonlinear complementarity functions, Adv. Model. Simul. Eng. Sci. 5 (1) (2018) 1–37.

[31] Alexander Seitz, Wolfgang A. Wall, Alexander Popp, Nitsche's method for finite deformation thermomechanical contact problems, Comput. Mech. 63 (6) (2019) 1091–1110.

[32] Alexander Popp, Mortar Methods for Computational Contact Mechanics and General Interface Problems (Ph.D. thesis), Technische Universität München, 2012.

[33] Caroline Danowski, Volker Gravemeier, Lena Yoshihara, Wolfgang A. Wall, A monolithic computational approach to thermo-structure interaction, Internat. J. Numer. Methods Engrg. 95 (13) (2013) 1053–1078.

[34] Francesc Verdugo, Wolfgang A. Wall, Unified computational framework for the efficient solution of n-field coupled problems with monolithic schemes, Comput. Methods Appl. Mech. Engrg. 310 (2016) 335–366.

[35] 4C, 4C: A Comprehensive Multi-Physics Simulation Framework, 2024, URL https://www.4c-multiphysics.org/. (Accessed: 16 June 2024).

[36] Caroline Danowski, Computational Modelling of Thermo-Structure Interaction with Application to Rocket Nozzles (Ph.D. thesis), Technische Universität München, 2014.

[37] M.A. Puso, T.A. Laursen, A mortar segment-to-segment contact method for large deformation solid mechanics, Comput. Methods Appl. Mech. Engrg. 193 (6–8) (2004) 601–629.

[38] Christoph Meier, Alexander Popp, Wolfgang A. Wall, Geometrically exact finite element formulations for slender beams: Kirchhoff–Love theory versus Simo–Reissner theory, Arch. Comput. Methods Eng. 26 (1) (2019) 163–243.

[39] A. Prakash, W.G. Nöhring, R.A. Lebensohn, H.W. Höppel, E. Bitzek, A Multiscale Simulation Framework of the Accumulative Roll Ronding Process Accounting for Texture Evolution, Mater. Sci. Eng. A 631 (2015) 104–119.

[40] Karol Frydrych, Katarzyna Kowalczyk-Gajewska, Aruna Prakash, On solution mapping and remeshing in crystal plasticity finite element simulations: application to equal channel angular pressing, Modelling Simul. Mater. Sci. Eng. 27 (7) (2019) 075001.

[41] M. Dittmann, F. Aldakheel, J. Schulte, F. Schmidt, M. Krüger, P. Wriggers, C. Hesch, Phase-field modeling of porous-ductile fracture in non-linear thermo-elasto-plastic solids, Comput. Methods Appl. Mech. Engrg. (ISSN: 0045-7825) 361 (2020) 112730.

[42] Sebastian D. Proell, Wolfgang A. Wall, A simple yet consistent constitutive law and mortar-based layer coupling schemes for thermomechanical macroscale simulations of metal additive manufacturing processes, Adv. Model. Simul. Eng. Sci. 8 (1) (2021) 1–37.

[43] Sebastian D. Proell, Wolfgang A. Wall, Christoph Meier, On phase change and latent heat models in metal additive manufacturing process simulation, Adv. Model. Simul. Eng. Sci. 7 (1) (2020) 1–32.

[44] Sebastian D. Proell, Peter Munch, Wolfgang A. Wall, Christoph Meier, A highly efficient computational approach for fast scan-resolved simulations of metal additive manufacturing processes on the scale of real parts, Additive Manufacturing 79 (2024) 103921.

[45] Xiaoye S. Li, An Overview of SuperLU: Algorithms, Implementation, and User Interface, ACM Trans. Math. Softw. 31 (3) (2005) 302–325.